PS451 Final Year Project

Pseudomagnetic Waveguides in Strained Graphene

Name: Cian Reidy

Student number: 17311803

Class: PHA4

Date: 29th March 2022

Supervisor: Dr. Stephen Power

Declaration

Name: **Cian Reidy**
Student ID Number: **17311803**
Programme: **PHA4**
Module Code: **PS451**
Assignment Title: **Pseudomagnetic Waveguides in Strained Graphene**
Submission Date: **29/03/22**

I understand that the University regards breaches of academic integrity and plagiarism as grave and serious.

I have read and understood the DCU Academic Integrity and Plagiarism Policy. I accept the penalties that may be imposed should I engage in practice or practices that breach this policy.

I have identified and included the source of all facts, ideas, opinions, viewpoints of others in the assignment references. Direct quotations, paraphrasing, discussion of ideas from books, journal articles, internet sources, module text, or any other source whatsoever are acknowledged and the sources cited are identified in the assignment references.

I declare that this material, which I now submit for assessment, is entirely my own work and has not been taken from the work of others save and to the extent that such work has been cited and acknowledged within the text of my work.

I have used the DCU library referencing guidelines (available at: http://www.library.dcu.ie/LibraryGuides/Citing&ReferencingGuide/player.html) and/or the appropriate referencing system recommended in the assignment guidelines and/or programme documentation.

By signing this form or by submitting this material online I confirm that this assignment, or any part of it, has not been previously submitted by me or any other person for assessment on this or any other course of study.

By signing this form or by submitting material for assessment online I confirm that I have read and understood DCU Academic Integrity and Plagiarism Policy (available at: http://www.dcu.ie/registry/examinations/index.shtml).

Name:_____*Cian Reidy*_____

Date:_____*29/03/22*_____

Contents

Acknowledgments

List of Figures

Abstract

Efficacious electron confinement and wave-guiding is pertinent to the further development of nano-scale technological devices. In recent times, novel fields such as *straintronics* has emerged in an endeavour to exploit the electronic transport regimes of effectively two-dimensional materials. In light of this, Graphene presents itself as an effectively two-dimensional, hexagonally shaped molecular allotrope of Carbon with exceedingly unique electronic properties. These unique properties have invoked a paradigm shift in fundamental physics, providing for a virtual coupling of condensed-matter physics and quantum electrodynamics. The emergence of quasi-relativistic fermions within the vicinity of the Fermi level provides for the basis of expressing graphene's energy states in the form of a Dirac-like Hamiltonian. This remarkable deduction is realised through the conventional Nearest-Neighbour-Tight-Binding (NNTB) formulation of graphene. In context of the application of geometric lattice strain, both conceptualisations prove fruitful in the extraction of novel electronic properties. In particular, the discussion throughout revolves primarily around inhomogeneous out-of-plane lattice strain modeled by several Gaussian functions. On one hand, as a consequence of strain, the continuum Dirac formalism predicts the emergence of pseudo-gauge (PGF), pseudo-magnetic fields (PMF) and scalar field potentials from the spatial dependency of the strain modulated hopping integral, whilst on the other hand, the NNTB formalism provides for the description of the strain modulated electronic transport properties within the system. The emergent strain fields provide for the ability to confine and control electron trajectories within the strain regions, with the manifestation of "snake-states" confined to regions of alternating pseudo-magnetic fields characterised by semi-classical cyclotron orbits. Certain strain regimes can be classified synonymously as "nano-wires" characterised by quantum conductance. Conclusively, the addition of strain induced PMFs subsequently induces the breaking of the local sub-lattice symmetry through the redistribution of the local density of states. This property implies for the existence of polarizable currents characterised by their valley indices.

1 Introduction

1.1 The Revelation of Graphene

Graphene's remarkable electronic structure has been theoretically studied for the greater part of 70 years [1], with its first conceptualisation demonstrated by P.R. Wallace in 1947 in his paper *"The Band Theory of Graphite"*, for which he sought an elucidation of graphite's inherent electronic properties. Wallace devised the electronic band structure of graphene by means of the "Tight binding" approximation [1], of which identical methodology is adopted hereout, as it constitutes the fundamental basis for describing the electron transport properties within graphene. Graphene, a derivative of graphite, is the term attributed to a two-dimensional, flat, mono-layer segment of carbon atoms, which are tightly bound into a honeycomb or hexagonal lattice configuration by carbon-carbon bonds, referred to as σ-bonds(see fig.). The intriguing electronic transport properties emergent in graphene are a consequence of the out of plane π-bonds, which form the band structure. Succeeding Wallace, was a shift towards experimental research, with several notable attempts occurring in the acquisition and observation of isolated graphene. In 1962 H. P. Boehm's group [2], whose work was a continuation of F. Vogt and G. Ruess's 1948 experiment; consisted of observing small, multi-layer graphene-oxide flakes of several nano-meters thick using transmission electron spectroscopy (TEM)[3]. Boehm's work, although controversial, realised the existence of monolayer graphite through the analysis of these small graphene-oxide flakes via TEM methods, for which he then later successfully coined the very term 'graphene' in the year of 1986 [4]. In addition, there were several other notable attempts to isolate graphene via epitaxial growth on various metal substrates; studies included those conducted by J. Grant demonstrating graphitic films created on Ruthenium and Rhodium [5] and the growth of such films on Nickel by J.M. Blakely [6]. In October 2004, A. Geim and K. Novoslev seceded in isolating mono-layer segments of graphene from bulk Graphite. There methods, belatedly simplistic, required some adhesive tape and some silica. The process by which the graphene was extracted is referred to as micro-mechanical cleavage or exfoliation [7], which involved the use of adhesive tape to remove layers of graphene from the graphite source. The graphene layers were then transferred to a silicon dioxide layer upon a silicon wafer, which interacted with the graphene fragments,separating them electrically. [7] [8].

1.2 A Brief Overview of the Emergent Electronic Properties in Graphene

The term graphene is attributed to a two-dimensional, flat, monolayer segment of Carbon atoms which are tightly bound via sp^2 orbital hybridization in a hexagonal primitive unit cell configuration [8]. Each consecutive Carbon atom is covalently bonded with the next by means of σ-bonds; providing for graphenes substantial tensile strength, possessing an estimated Young's modulus of 2.4 ± 0.5 Tpa [9]. However, responsible for graphenes rather exotic electronic properties are the remaining 2p orbitals, referred to as π-bonds, which are orientated orthogonally to the basal plane and form graphenes respective conductance and valence bands through orbital hybridization with neighbouring π-bonds. These bands, also known as the π-band and π^*-bands, converge at each of the six Dirac points (the **K** and **K'** points) located on the vertices of the Brillouin zone in momentum space, making graphene in its pristine configuration a zero-gap material [10]. The electronic band structure of solid materials, in the general sense is elucidated by the correspondence between the energy and momentum of valence electrons. One particular way of realising this structure is through the application of the tight binding approximation alluded to earlier. In context of monolayer graphene, we have the confinement of the valence electrons to a two-dimensional plane, therefore we have the confinement of its corresponding momentum space to only two-dimensions. Observing graphene's electronic band structure near the Dirac points exhibits an energy-momentum dispersion regime which is linear in accordance to the geometry of the Dirac cones; which is approximately equivalent to an electron having a Dirac energy of 1eV [10]. This linearity is a consequence of the Fermi-surface, or band structure, taking a conical shape at these low energies. In this particular regime, the charge carriers become 'quasi-relativistic', as their effective masses reduce to zero, and their velocities approach a Fermi-velocity approximately 0.003c [10-12]. Due to the relativistic nature of the charge carriers, the system can be formally de-

scribed by a two-dimensional analogue of the Dirac equation as opposed to the conventional Schrödinger approach. Consequentially, there is the emergence of chirality regarding the pseudospin-states of the charge carriers due to the symmetry of the band structure about the Dirac points (**K** and **K'** points). This chiral property emanates from the orientation of the 'spin' component which dependent on the direction of propagation of the charge carrier i.e, whether the charge carrier moves above or below its respective **K'** or **K'**. So, for example, we have 'spin-up' particles corresponding to charges propagating above K, and similarly 'spin-down' particles corresponding to propagation below the **K** point. For the **K'** points, we have the same dynamics now with an opposing helicity, which implies that we can have two in-equivalent charge carriers from different valleys with opposing pseudo-spin states [13-14]. This property bears significance due to its implications on the electronic transport properties in graphene, where applications can be sought in the storing and transferring of information in Dirac based spintronic materials [14-15]. However, an important distinction must be outlined regarding the properties of the pseudo-spin outlined. Typically the transport of real electron spin can be induced by a real magnetic field, however, for the case of pseudo-spin, its interpretation is more subtle. The pseudo-spin regards the degree of freedom associated with the in-equivalent valleys within the sub-lattice site. For its analogous polarization; in certain contexts of strain, its interaction with a pseudo-magnetic field causes sub-lattice symmetry breaking, therefore effectively "polarizing" the pseudo-spin associated with each valley region. [15].

Just to further emphasise the significance of graphene's intrinsically unique properties, these emergent 'quasi-relativistic' characteristics provide for a rather tangible coupling between condensed-matter physics and quantum electrodynamics (QED); where once rather exotic properties pertinent to high energy QED can now be simulated in laboratory environments [13][16-17]. For instance, The manifestation of charge-conjugation symmetry quintessential to relativistic fermions give rise to the distinctive klein-paradox at minute energies; which in contrast would require extremely large electric fields induced from energies surplus of $\approx mc^2$ [17]. For context, I quote M.Katsnelson, K. Novoselov and A. Geim's paper: *"Chiral tunnelling and the Klein paradox in graphene"* verbatim, which exclaims: " Indeed, its observation (Klein tunnelling) requires a potential drop of $\approx mc^2$ over the Compton length $\hbar/mc$ which yields enormous electric fields ($\varepsilon > 1016V\,cm^{-}1$) and makes the effect relevant only for such exotic situations as, for example, positron production around super-heavy nuclei with charge Z 170 or evaporation of black holes through generation of particle–antiparticle pairs near the event horizon" [17].

1.3   Properties of Lattice Strain in Graphene

The imposition of geometric lattice strain on graphene systems has beared rather compelling results regarding the electronic band structure and electron transport properties within graphene systems. Firstly, In the context of homogeneous uni-axial lattice strain, numerous studies have demonstrated the formation of a exploitable transport gap in graphene, which typically isn't present in its pristine configuration [18-20]. Tight-binding models and ab initio calculations corresponding to uni-axial strained systems displayed the migration of the Dirac cones away from their symmetry **K** and **K'** points located in the Brillouin zone at strains < 20%, whereas strains exceeding this along the zig-zig direction produced transport gaps. Higher strains caused

substantial anisotropy corresponding to the the hopping integral terms related to each sub-lattice sites. The anisotropic hopping integrals due to the lattice deformation causes a migration of the Dirac cones from their symmetry points (**K** and **K'** points) and the degree of their relative magnitudes and the direction of which the stain is imposed on the graphene system has subsequent influence on which direction the cones shift. A much more quantitative and explicative case is developed by L. Yang and J. Han in their paper *"Electronic Structure of Deformed Carbon Nanotubes"* [21]. Conclusively, it has been shown that an exploitable band gap emerges in uni-axial strained graphene due to the merging of in-equivalent Dirac cones along zigzag directions and similarly, identical effects have been discovered for shear straining [20].

Secondly, and more pertinent to this project is the imposition of in-homogeneous, out of plane lattice strain in graphene. These particular straining parameters result in a change in the electron hopping integral between neighbouring carbon atoms corresponding to in-equivalent lattice sites referred to as the A and B points in accordance with nomenclature. The Fourier transform of these points correspond to the **K** and **K'** points in momentum-space or reciprocal-space as previously elucidated. To clarify, the hopping integral term is an expression which describes the electronic coupling of neighbouring lattice sites; providing a minimum energy value required for electrons associated with one site to "hop" to its neighbouring site. The change of expression of the hopping integral, as a consequence of strain, has the equivalent theoretical description of a gauge field from which emerges a vector potential that is analogous to that of a magnetic field [22]. This vector potential emerges only in the explicit case of inhomogeneous strain, where the spatial dependency within the pseudo-gauge expression implies a non-vanishing curl. This vector potential is conventionally referred to as the pseudo-magnetic field (PMF) and modifies the properties of the electronic transport by virtue of the Lorentz force as if it were a real magnetic field. Furthermore, unlike real magnetic fields, the induced pseudo-magnetic fields preserve the time-reversal symmetry as briefly implied earlier. The effective Dirac Hamiltonian has opposing signs in each respective **K** and **K'** valleys, therefore, the induced pseudo-magnetic field has opposing directions corresponding to the electrons which originate from each valley. This property can be associated with a new additional degree of freedom corresponding to the origins of the charge-carriers; which can be exploited to produce valley-polarized currents [23-24].

1.4   Applications of Straintronics in Valleytronic devices

The prevailing motivation behind imposing strain in graphene systems is primarily due the plethora of applications available in graphene based electronics. Graphene incorporates characteristics of metals and semi-conductor materials; making it a rather intriguing replacement for the conventional silicon based conductors of today [25]. Such favourable intrinsic properties for ballistic transport in graphene include its immensely low resistivity, which is $\approx 1.0\ \mu\Omega\ cm$ and its very high electron mobility $\approx 15000\ cm^2\ V^{-1}s^{-1}$, which is an order of magnitude higher in contrast with silicon $\approx 1400\ cm^2\ V^{-1}s^{-1}$ [25-27]. The application of strain-engineering to graphene structures seems to be a promising approach for valleytronic devices. Valleytronic devices, analogous to spintronic devices, differ in their mechanism by instead, exploiting the valley degree of

freedom associated with the local extrema of the electronic band structure in certain crystalline materials. The information is now encoded corresponding to the quasi-momentum associated with the charge carriers emanating from a particular valley region [28]. In context of strained graphene, more specifically, in-homogeneously strained graphene as mentioned earlier, we have significant distortion of the lattice structure which induces a spatially varying pseudo-magnetic field. The conservation of the time-reversal symmetry implied by the directional disparity of the PMF constitutes the framework for manipulating the valley degree of freedom in strain-based graphene electronics [29]. Moreover, it has been demonstrated that introducing a real external magnetic field in addition to the strain induced PMFs can also produce *bulk polarized currents* due to the greater interaction between the two fields generating a separation in space and energy corresponding to the states from each valleys [30].

2 Theoretical Discussion

To provide an overview; The fundamental approach to investigating graphene's intrinsic electronic structure can be established on the basis of two formulations [31], firstly, the nearest neighbour tight-binding approximation (NNTB)(see. **Sec. 2.2.3**), and secondly, the continuum Dirac model. The latter formulation can be derived from the former by analysis of the eigen-spectrum close to the Dirac points (see. **Sec. 2.3**). The NNTB model in graphene provides for a description of the electronic band structure formed by the valence electrons that correspond the orthogonal p_z orbital. Each Carbon atom within the structure contributes a p_z out of plane orbital, constituting an orthonormal basis set from which once can obtain the tight-binding Hamiltonian matrix [31]. There exists additional matrix terms such as the "hopping integral", t, which emerges due to the uncertainty of the electron being in either sub-lattice 'A' or 'B' and the "overlapping integral", corresponding to the overlapping of the orbital wave-functions. The contributions of the latter term are considered negligible throughout. The set of eigen-pair solutions of the tight-binding Hamiltonian will render the electronic band structure and corresponding available eigen-states (see. **Sec. 2.2.3** and **Sec. 3.1**). The emergence of the 'quasi-relativistic' properties regarding the charge carriers is a consequence of reducing the tight-binding Hamiltonian to an effectively massless 2D Dirac-like Hamiltonian about the **K** and **K'** points. The eigen-pair solutions for this Dirac-like Hamiltonian will provide the eigen-vectors corresponding to the energy states above or below the **K** and **K'** with eigen-states described by a linear dispersion regime (see. **Sec. 2.3.1**) [31-32]. Due to the strong relationship between graphenes morphology and electronic structure, imposing inhomogeneous out of plane strain subsequently changes the hopping integral matrix terms corresponding to the tight-binding Hamiltonian. The real space structure becomes deformed according to the strain parameters, and the pristine electronic structure ultimately changes. The continuum Dirac model predicts the presence of pseudo-gauge fields **A** and a pseudo-scalar potential Φ, as a consequence of the change in the hopping integral matrix terms and a change in charge distribution respectively [34-35]. These pseudo-gauge fields perturb the Dirac-like Hamiltonian and appear in the off diagonal matrix element terms. (see. **Sec. 2.4.2**) [33]. Due to the the spatial dependency pseudo-gauge fields, which are described by the general strain tensor, the presence of pseudo-magnetic fields (PMFs) emerge, with the property

of time-reversal symmetry conservation due to opposing negative and positive regions depending on its valley origin [34]. The transport of the charge-carriers can be described by quasi-classical cyclotron orbits due to the emergent perpendicular pseudo-magnetic fields [37]. The relative directional disparity of these PMFs produce 'snake states' at the interface between the opposing field directions (see. **Sec. 3.3**)[34-37]. Amongst a plethora of possibilities, these snake states can be utilised to direct the flow of charge carries in graphene with considerable efficiency, even at low magnetic fields. [37-38]

2.1 The Intrinsic Physical Structure of Monolayer Graphene

Alluding to the previous section, graphene's primitive unit cell is comprised of six Carbon atoms residing in a two-dimensional hexagonal bravais lattice configuration. Graphene structures extended into a monolayer plane comprises of four chemical-bond formations, three of which are in-plane covalent bonds with neighbouring Carbon atoms, which take the form of σ-bonds; and the fourth being the out-of-plane π-bond [10][31]. The consequence of this chemical bonding structure of graphene in conjunction with its lattice configuration is truly what gives rise to its rather unique electronic properties.

2.1.1 The Chemical Bonding Structure

The atomic ground-state configuration for Carbon has the form $1s^2 2s^2 2p^2$, with two electrons confined to the 1s orbital and the remaining four divided between the 2s and $2[p_x, p_y, p_z]$ orbitals, However, in circumstances where other atoms are present, such as within graphene's lattice structure, we have a succession of covalent bonds between each Carbon atom. This has the implication that electrons from the 2s orbital exists as a quantum state superimposed with two of $2[p_x, p_y, p_z]$ orbital quantum state, in whats referred to as a sp^2 hybridised state. These covalent bonds are what forms graphenes σ-bonds. Considering the hybridised sp orbital is some linear superposition of two quantum states, namely the 2s and p_x, p_y or p_z orbital, one can represent the hybridised state conventionally by allowing the σ-bonds to form the x and y plane (basal plane) and the π-bonds to be orthogonal to such, pointing in the z direction. One can expand the expressions of the sp^2 orbital wave-functions on the basis of the 2s and $2[p_x, p_y, p_z]$ Hilbert space. Figure 1. below provides a visual representation of the orbitals in three dimensional space, where **(a)** Isolated Carbon with un-hybridised bonds, **(b)** Carbon in the presence of other Carbon atoms, constitute the hybridised sp^2 bonds and **(c)** monolayer graphene comprising of the σ and π-bonds.
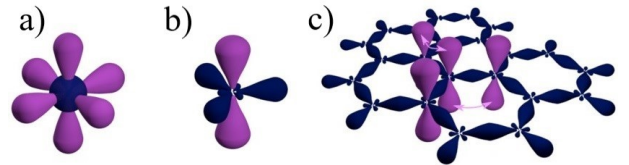
Figure 1. (a) Un-hybrisdised Carbon , where the blue shell corresponds to the 2s orbital and the purple lobes correspond to the $2[p_x, p_y, p_z]$ orbitals. **(b)** The blue lobes correspond to the hybridised sp^2 orbitals and the purple lobes represent the single p_z orbital **(c)** Monolayer graphene with σ (blue) and π-bonds (purple). [40]

The remaining $2p_z$ orbital forms what is known as the π-bond. These bonds are hybridised with the other π-bonds located on each of the neighbouring Carbon atoms, and collectively form

the π-band and the $\pi*$-bands, all of which exist orthogonally to the σ-bonds located on the basal plane as mentioned previously [10]. The corresponding electronic wave-function can be represented in the Bloch formulation [39], which forms an orthonormal eigen-basis set with the Hamiltonian of the system, and therefore can be expanded as a linear combination of all the contributing wave-functions associated with the system, whose eigen-solutions will form the electronic band structure of graphene. The premise of the Bloch formulation is outlined explicitly in **Sec. 2.2**.

2.1.2   The Lattice Structure in Real Space

Graphene's two-dimensional hexagonal lattice configuration formed by the sp^2 hybridised orbitals, comprises of a primitive unit cell referred to as the bravais lattice [31]. The basis of graphenes bravais lattice is formed at the sub-lattice points of two neighbouring Carbon atoms which have a typical bond length of 1.42Å[10][31]. These sub-lattice points are conventionally labelled the 'A' and 'B' and remain nonequivalent under linear transformations. (See figure 1.1.) The primitive lattice vectors a_1 and a_2 expanded upon either sub-lattice point 'A' or 'B' span a two-dimensional subspace forming a triangular Bravais lattice. Any linear combination of these basis vectors will essentially yield a triangular subspace with a total dimension equivalent to the degree n. An imperative point to note here is that due to the inability to connect lattice sites 'A' and 'B' through any unitary vector translation, a linear combination of unit vectors a_1 and a_2 will only yield lattice points corresponding to a single sub-lattice 'A' or 'B'[41].

Consider the following representation of graphene oriented such that its "arm-chair" direction is adjacent to the x-axis and its "zig-zag" direction is adjacent to the y-axis. The lattice vectors are expanded in the vector space spanned by Both the x and y axes which form an orthogonal basis.

$$a_1 = \left(\frac{3a}{2}, \frac{\sqrt{3}a}{2}\right), \quad a_2 = \left(\frac{3a}{2}, -\frac{\sqrt{3}a}{2}\right) \qquad (1)$$

$$\delta_1 = \left(-\frac{a}{2}, \frac{\sqrt{3}a}{2}\right), \quad \delta_2 = \left(-\frac{a}{2}, -\frac{\sqrt{3}a}{2}\right),$$

$$\delta_3 = (a, 0) \qquad (1.1)$$

Equation 1. provides the lattice vectors corresponding to some arbitrarily selected atomic basis i.e. either 'A' or 'B'. In context of this diagram, the origin of the orthogonal x,y basis coincides with the intersection of the a_1 and a_2 vectors. Equation 1.1 provides the vectors connecting nearest neighbouring sites with its basis origin also located at the point of intersection of each vector. Determining the modulus of a_1 using Pythagoras: $\left(\frac{3a}{2}\right)^2 + \left(\frac{\sqrt{3}a}{2}\right)^2 = |a_1|^2 \Rightarrow a_1 = \sqrt{3}a$, where a is the carbon-carbon bond length of ≈ 1.42Å, Therefore, $a_1 = 2.46$Å. Having knowledge of this, the area of the primitive bravais cell can be determined, $A = \frac{\sqrt{3}a^2}{2} = 0.051 \ nm^2$ and thus, the density of Carbon can be estimated, $n = 2/A = 3.9$ x $10^{15} \ cm^{-2}$ [10][31]. The real space lattice structure is outline in **Figure 1.1**, with the equivalent sub-lattice sites being connected by the blue-arrows (a_1, a_2) and the nearest neighbouring sites in purple $\delta_1, \delta_2, \delta_3$. This method relates to the formation of the triangular Bravais unit cell, however, one can represent the lattice structure using conventional cell methods or perhaps some exhaustive linear

mapping function which uses an arbitrary combination of lattice vectors to represent all the lattice points in the entire subspace. (This method is employed in **sec. 3** for a more effective implementation).
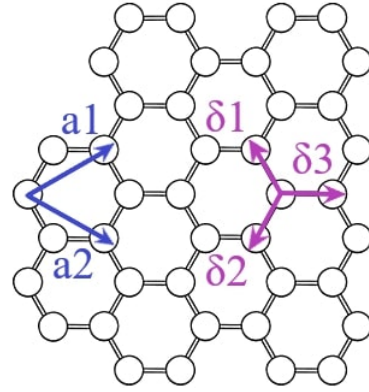
Figure 1.1. Real space monolayer graphene lattice structure with primitive lattice vectors a_1 and a_2 spanning the triangular bravais lattice subspace. δ_1, δ_2 and δ_3 connect nearest neighbour sub-lattice points 'A' and 'B'

2.1.3   The Lattice Structure in Reciprocal Space

The reciprocal lattice structure (Figure 1.2) is achieved via the Fourier transformation of the real space lattice structure from real space to Fourier space (K - space). The structure can now be represented by the primitive reciprocal lattice vectors seen in equations 1.4, 1.5. In real space, the lattice vectors reflect the intrinsic spacial periodicity of the lattice structure. Equivalently, the reciprocal space vectors represent wave-vectors of plane-waves at each lattice point, whose periodicity is identical to the real space function [31][41]. In the general case, Determination the reciprocal lattice vectors in the two-dimensions can be achieved by the relations:

$$b_1 = \frac{2\pi}{|a_1 \times a_2|} \begin{bmatrix} a_{2,y} \\ -a_{2,x} \end{bmatrix} \qquad (1.2)$$

$$b_2 = \frac{2\pi}{|a_1 \times a_2|} \begin{bmatrix} -a_{1,y} \\ a_{1,x} \end{bmatrix} \qquad (1.3)$$

Therefore:

$$b_1 = \begin{bmatrix} \frac{-8\pi}{3\sqrt{3}a^2}, \frac{-8\pi}{3\sqrt{3}a^2} \end{bmatrix} \begin{bmatrix} -\sqrt{3}a/2 \\ -3a/2 \end{bmatrix} = \begin{bmatrix} \frac{4\pi}{3a}, \frac{4\pi}{\sqrt{3}a} \end{bmatrix} \qquad (1.4)$$

$$b_2 = \begin{bmatrix} \frac{-8\pi}{3\sqrt{3}a^2}, \frac{-8\pi}{3\sqrt{3}a^2} \end{bmatrix} \begin{bmatrix} -\sqrt{3}a/2 \\ 3a/2 \end{bmatrix} = \begin{bmatrix} \frac{4\pi}{3a}, -\frac{4\pi}{\sqrt{3}a} \end{bmatrix} \qquad (1.5)$$

This satisfies the conditions $a_1 b_1 = a_2 b_2 = 2\pi$ and $a_1 b_2 = a_2 b_1 = 0$ or in the general case $a_i b_j = 2\pi \delta_{ij}$ where $i, j = 1, 2$ between the direct and reciprocal lattice vectors [31]. The physical significance of this corresponds to the relationship between a set of plane waves, whose corresponding wave vectors k span the entire subspace of the Bravais lattice with the equivalent periodicity. Thus, as a consequence, this implies that relation between the set of plane-waves propagating within the reciprocal lattice with corresponding wave-vectors k, will have a total phase shift $k \cdot R$, up to a multiple of 2π relative to the origin and some point R on the direct lattice [10][31]. This gives rise to the Brillouin zone (**BZ**) and the **K** and **K'** or Dirac points located at each vertices of the reciprocal space lattice (**Figure 1.2**). These points are divided into two non-equivalent sets of three points i.e. they cannot be accessed via a reciprocal unit

vector. The two non-equivalent **K** and **K'** points displayed in **figure 1.2** can be expressed by the vectors in reciprocal space:

$$K = \left(\frac{2\pi}{3a}, \frac{2\pi}{3\sqrt{3}a}\right) \quad K' = \left(\frac{2\pi}{3a}, -\frac{2\pi}{3\sqrt{3}a}\right) \quad (1.6)$$
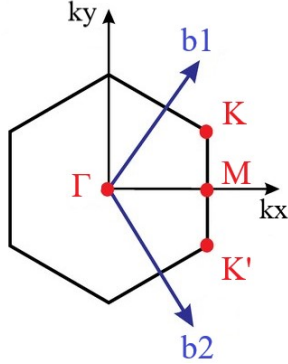
The corresponding Brillouin zone is illustrated below:

Figure 1.2. Reciprocal space configuration of graphene forming the first Brillouin zone (**BZ**) with the reciprocal lattice vectors described by b_1 and b_2. The Dirac points correspond to the **K** and **K'** points which separated by midpoint **M**. Each **K** and **K'** (expressions 1.6)

Observing all **K** and **K'** points in the diagram, its clear that for each Dirac point corresponds to another, in-equivalent Dirac point through a reflection symmetry, provided the we utilise the orthogonal basis spanned by k_x and k_y situated at origin Γ. Thus, the most rudimentary way of obtaining relative Dirac points is through the relation $R v_{K,K'}$, where R is just a rotational matrix, corresponding to $\theta = \pi$, which functions simply by exchanging signs of the vector components. $v_{K,K'}$ corresponds to the vector representing either **K** or **K'**. From the two points above, one can achieve four of six relative locations of each Dirac point. The remaining two will require a prerequisite rotational transformation of either **K** or **K'** to its neighbour. The significance of these crystallographic points becomes apparent in the following sections, when investigating the dispersion regime through the NNTB methodology at energies close to the Fermi-level.

2.2   The Electronic Band Structure

As first postulated by P.R. Wallace in 1947 [1], the Electronic band structure of graphene can be achieved by the application of the nearest-neighbour tight binding approximation, more precisely however, application of the tight-binding approximation to the $|p_z\rangle$ orbitals, or the π-bonds explicitly gives rise to graphenes conduction and valence bands, which are demonstrated to coalesce at the six Dirac points or **K** and **K'** on the vertices of the Brillouin zone in reciprocal space. As alluded to earlier, the σ electrons forming strong covalent in-plane σ-bonds correspond to energy-bands which form considerably far away from the Fermi-energy, thus they can be sufficiently neglected in the formulation of the tight-binding model [42] To briefly overview, the tight binding model is a quantum mechanical model that involves the application of the Schrödinger equation to a periodic system of tightly bound atoms. The Hamiltonian is projected onto the basis of the atomic orbitals which are constructed of Bloch sums that become the basis for which the the electronic wave-functions are expressed in. These basis functions form the Hilbert space, which is assumed to be orthonormalised, allowing for the extraction of the eigen-solutions which constitute the electronic band structure of the

system. In the context of solids, the composition of the Hamiltonian is now specifically parameterised to reflect the periodicity of the atomic potentials, meaning the potential component of the Hamiltonian will be a summation over the lattice vectors of each atomic potentials corresponding to each site, which has the general form:

$$V(\mathbf{r}) = \sum_{\mathbf{R}} V_{at}(\mathbf{r} - \mathbf{R}) \quad (1.8)$$

Which is say, periodic through the translation $\mathbf{R}'$:

$$V(\mathbf{r}) = \sum_{\mathbf{R}} V_{at}(\mathbf{r} - (\mathbf{R} - \mathbf{R}'))$$

$$V(\mathbf{r}) = \sum_{\mathbf{R''}} V_{at}(\mathbf{r} - \mathbf{R}'') \quad (1.9)$$

Where $\mathbf{R} - \mathbf{R}' = \mathbf{R}''$ is just a translation vector over all possible lattice vectors. Therefore the crystal Hamiltonian takes the general form:

$$H = -\frac{\nabla^2}{2m} + \sum_{\mathbf{R''}} V_{at}(\mathbf{r} - \mathbf{R}'') \quad (1.10)$$

Implicit here is the sum of all individual contributing Hamiltonians corresponding to every atomic site confined to the system [44]. The bound-states, or eigen-states and corresponding eigen-functions are obtained by solving the eigen-value problem in the basis of the Bloch functions. Furthermore, considering nearest neighbouring atoms, or the in-equivalent 'A' and 'B' sub-lattice points; and additional "hopping integral matrix" term emerges due to the occurrence of electrons from 'A' having sufficient energy to 'hop' to 'B' and vice-versa [10][13][31]. There also exists the "overlap integral matrix" term, which in this context isn't sufficient enough to consider, however it exists due to the overlapping of electronic wave-functions from neighbouring sites.

2.2.1   The Nearest Neighbour Tight Binding Hamiltonian - Finite Formulation

Conversely, as a brief aside, In the context of the real space lattice structure, constituting a finite system of pristine monolayer graphene, the Hamiltonian matrix can be constructed by a large finite tridiagonal matrix (2.1), with its diagonal elements corresponding to the onsite energies ε and the off-diagonal elements corresponding to hopping integral elements γ_0. This can be described by the summation over states:

$$H = \sum_{i} |i\rangle \varepsilon_i \langle i| + \sum_{\langle i,j \rangle} |j\rangle \gamma_{ij} \langle j| \quad (1.11)$$

Typically, for pristine systems ε_i remains constant along with γ_{ij}. The γ_{ij} terms only concerns nearest neighbouring atoms ij over the summation. This particular method is useful as it provides for a discrete implementation of the Hamiltonian computationally, for which a large matrices can be constructed and diagonalized, to evaluate the eigen-spectra of a finite segment of graphene. For larger systems, the Bloch formulation outlined below is appreciated.

2.2.2   The Bloch Formulation

Considering the crystalline structure of graphene as being some periodic potential, whose periodicity corresponds to that of the crystal structure; Then Bloch's theorem states that the solutions of the Schrödinger equation applied to the electron states in the lattice are in the form of plane waves, whose wave-vector components are modulated by some periodic function that correspond to the potential [43]. Considering now that the Bloch

function reflects the transnational symmetry of the lattice, it serves as a suitable basis for constructing the trial wave-function necessary to project the tight-binding Hamiltonian.

Firstly, we consider the Bloch function case for a singular sub-lattice point (a), in a perfect crystal. In this context, once again, the trial wave-function constitutes of the atomic orbital wave-functions which corresponds to the equivalent sub-lattice sites in question $\phi_{(a)}(r-R_i)$ [42-44]. The trial wave-function must conserve the discrete translational symmetry of the lattice, thus there must exist some some operator Υ_{R_i} that enables one to shift every wave function by some amount R_i, where R_i is the lattice vector, considering only 2-D real space this takes the form: $R_i = a_1 n_1 + a_2 n_2$. Therefore, we have an operator which takes the expression:

$$\Upsilon_{R_i} = e^{ik \cdot R_i} U(r) \qquad (1.12)$$

The application of this operator through any arbitrary R_i leaves the physical system invariant, due to the lattice sites being equivalent. Consequently, the symmetry operator Υ_{R_i} commutes with the Hamiltonian $H \Rightarrow [\Upsilon_{R_i}, H] = 0$, such that it forms a simultaneous eigen-basis. This implies that the eigen-states corresponding to Υ_{R_i} are also necessarily eigen-states of the Hamiltonian, which correspond to the energy levels of the lattice system. The eigen-states also form Bloch states as they also correspond to the eigen-states of Υ_{R_i} [42][45]. Finally, every symmetry operator that exists, Υ_{R_i} commutes with every other possible symmetry operator Υ_{R_j} in the system, also forming a simultaneous eigen-basis. This is particularly useful in the case of multiple atoms per unit cell.

Therefore, the trial wave-function in the context of a singular sub-lattice point of dimension N takes the form:

$$\psi_k = \frac{1}{\sqrt{N}} \sum_{R_i}^{N} e^{ik \cdot R_i} \phi_{(a)}(r-R_i) \qquad (1.13)$$

where $\frac{1}{\sqrt{N}}$ normalises the wave-function. Therefore, we can see by projecting the Hamiltonian onto this basis, one can uncover the eigen-spectra corresponding to the energy of the lattice system. The subsequent section employs this concept to graphenes 2 atomic base bravais lattice to obtain the Tight-binding Hamiltonian.

2.2.3 The Nearest Neighbour Tight Binding Hamiltonian - Bloch Formulation

Graphene's unit cell consist of two in-equivalent **'A'** and **'B'** points. unlike the formulation above, we must now consider an additional sub-lattice point which cannot be related to its neighbour via any linear transformation that still preserves the symmetry operation, implying $[\Upsilon_R, H] \neq 0$ [45]. However, considering the fact that the **'A'** and **'B'** points are geometrically equivalent, there exists an identical symmetry operation for sub-lattice **'B'**, which commutes with the symmetry operation corresponding with **'A'**, such that $[\Upsilon_{R_i}, \Upsilon_{R_j}] = 0$, therefore the eigen-states of each are equivalent. In the case, the formation of the Hamiltonian matrix, omits the overlap matrix as it is sufficiently negligible [45], and therefore, only the expectation values corresponding to the **'A'** and **'B'** sites i.e $\langle \psi_A | H | \psi_A \rangle$, $\langle \psi_B | H | \psi_B \rangle$, in conjunction with the interaction of each sites i.e $\langle \psi_A | H | \psi_B \rangle$, $\langle \psi_B | H | \psi_A \rangle$ is considered. The term $\psi_{A,B}$ is the trial wave-function composed of the Bloch sums. Therefore, the Hamiltonian takes the rudimentary form:

$$H = \begin{pmatrix} \langle \psi_A | H | \psi_A \rangle & \langle \psi_A | H | \psi_B \rangle \\ \langle \psi_B | H | \psi_A \rangle & \langle \psi_B | H | \psi_B \rangle \end{pmatrix} \qquad (1.14)$$

Implicit in this is such that each expectation value is determined over the entirety of the lattice structure of dimension N, with the consideration of the nearest neighbour contributions for the off diagonal matrix elements. This is elucidated further in the explicit case for graphene below.

Before explicitly applying the theorem to graphenes system, it may be useful to expand upon section 2.2.2 by defining the general Bloch function for a system comprised of n orbitals. Each orbital is indexed by the notation "j", where "j" $\in \mathbf{N}$ and $i = 1...N$. The Bloch function is dependent on the position "r" and the wave-vector "k" and can be constructed by the following function [31][43].

$$\Phi_j(k,r) = \frac{1}{\sqrt{2}} \sum_{i=1}^{N} e^{ik \cdot R_{j,i}} \phi_j(r-R_{j,i}) \qquad (1.15)$$

This can be expanded as a linear superposition of a composite of Bloch functions with the expansion coefficient being $c_{j,l}$, representative of the projection of the wave-function onto the basis function.

$$\Psi_j(k,r) = \sum_{l=1}^{n} c_{j,l}(k) \Phi_l(k,r) \qquad (1.16)$$

$\Psi_j(k,r)$ is expanded in the basis of $\Phi_l(k,r)$, therefore the projection of the Hamiltonian onto this basis will yield the energy $E_j(k)$ of the "jth" band:

$$\langle \Psi_j | E_j(k) | \Psi_j \rangle = \langle \Psi_j | H | \Psi_j \rangle \Rightarrow$$

$$E_j(k) = \frac{\langle \Psi_j | H | \Psi_j \rangle}{\langle \Psi_j | \Psi_j \rangle} \qquad (1.17)$$

Considering the "Overlap" term is neglected, the trial wave-function forms an orthonormal basis and the term $\langle \Psi_j | \Psi_j \rangle = 1$. Substituting equation (1.16) into (1.17) yields:

$$E_j(k) = \frac{\sum_{i,l}^{n} c_{ji}^* c_{jl} \langle \phi_i | H | \phi_l \rangle}{\sum_{i,l}^{n} c_{ji}^* c_{jl}} \qquad (1.18)$$

As discussed, the Hopping integral matrix element between orbitals, in the general case, indexed "i" and "l":

$$H_{i,l} = \langle \phi_i | H | \phi_l \rangle \qquad (1.19)$$

$$= \frac{\sum_{i,l}^{n} c_{ji}^* c_{jl} H_{i,l}}{\sum_{i,l}^{n} c_{ji}^* c_{jl}} \qquad (1.20)$$

Holding "i" fixed and partially differentiating (1.18) via the quotient rule with respect to c_{ji}^* to find the local minima of E_j from which one can finally construct the general matrix equation or eigen-value equation which yields the electronic band structure.

$$\frac{\partial E_j}{\partial c_{jm}^*} = \frac{\sum_{i,l}^{n} c_{ji}^* c_{jl} \sum_{i,l}^{n} c_{jl} H_{i,l} - \sum_{i,l}^{n} c_{ji}^* c_{jl} H_{i,l} \sum_{i,l}^{n} c_{jl}}{(\sum_{i,l}^{n} c_{ji}^* c_{jl})^2}$$

$$\rightarrow \frac{\sum_{i,l}^{n} c_{ji}^* c_{jl} \sum_{i,l}^{n} c_{jl} H_{i,l}}{(\sum_{i,l}^{n} c_{ji}^* c_{jl})^2} - \frac{\sum_{i,l}^{n} c_{ji}^* c_{jl} H_{i,l} \sum_{i,l}^{n} c_{jl}}{(\sum_{i,l}^{n} c_{ji}^* c_{jl})^2} = 0 \qquad (1.21)$$

Equation (1.18) is embedded in the second term of (1.21), therefore, the equation reduces down to the following:

$$\sum_{l=1}^{n} H_{il} c_{jl} = E_j \sum_{l=1}^{n} c_{jl} \qquad (1.22)$$

Which can be expressed as a n dimensional matrix equation, where n is the quantity of atomic orbitals. Therefore, we can express this as the eigenvalue problem below:

$$H\psi_j = E_j\psi_j \tag{1.23}$$

Thus, E_j can be determined by the secular equation:

$$det(H_j - E_j) = 0 \tag{1.24}$$

[31][43-45]

2.2.4   The Diagonal Matrix Elements

Applying this to graphenes structure, firstly, Using the Bloch function from equation (1.15), we substitute it into the Hopping matrix H_{il}, under the assumption $i = j$ ('**A**' or '**B**' sites), such that $e^{ik\cdot(R_{1,j}-R_{1,i})} = 1$. Only contributions corresponding the wave function of equivalent sub-lattice points are considered. In the case below, point '**A**' is considered. The following diagonal elements of the H_{il} matrix are obtained from:

$$H_{A,A} \approx \frac{1}{N}\sum_{i=1}^{N}\langle\phi_A(r-R_{A,i})|H|\phi_A(r-R_{A,i})\rangle \tag{1.25}$$

$$\langle\phi_A(r-R_{A,i})|H|\phi_A(r-R_{A,i})\rangle = \varepsilon_{2p} \tag{1.26}$$

$$H_{A,A} \approx \frac{1}{N}\sum_{i=1}^{N}\varepsilon_{2p} = \varepsilon_{2p} \tag{1.27}$$

So, the first entry in the H_{il} matrix is equivalent to the onsite energy corresponding the the 2p orbital located at sub-lattice point 'A'. Equivalently, due to the lattice symmetry and the identicality of the Carbon atoms, the second main-diagonal element corresponding the the 'B' sub-lattice has an identical value, thus: $H_{A,A} = H_{B,B} = \varepsilon_{2p}$.

2.2.5   The Off-Diagonal Matrix Elements

The procedure is repeated for the off-diagonal elements which gives rise to the 'hopping' term associated with electrons transferring to neighbouring sub-lattice points. The considerable difference from the latter is that the orbital wave-functions from neighbouring sub-lattice points now have a contribution. More precisely, if we consider the sub-lattice point '**A**', where now we have the condition that $i \neq j$, its true that point '**A**' has three subsequent neighbouring '**B**' atoms, thus we can construct the matrix elements by considering the main orbital at lattice point '**A**' in conjunction with the orbitals associated with the neighbouring '**B**' points, indexing each with notation 'l', (l = 1, 2, 3) [31][45]:

$$H_{A,B} \approx \frac{1}{N}\sum_{i=1}^{N}\sum_{l=3}^{3} e^{ik(R_{B,l}-R_{A,i})}\langle\phi_A(r-R_{A,i})|H|\phi_B(r-R_{B,l})\rangle \tag{1.28}$$

The hopping integral is set to some parameter, $\langle\phi_A(r-R_{A,i})|H|\phi_B(r-R_{B,l})\rangle = -\gamma_0$, which are identical at all neighbouring sites, thus we can reduce the matrix element term into:

$$H_{A,B} \approx -\frac{1}{N}\sum_{i=1}^{N}\sum_{l=1}^{3} e^{ik(R_{B,l}-R_{A,i})}\gamma_0 \tag{1.29}$$

Where we can now define $f(k)$, which is just a summation over the phase terms of the orbitals at the three neighbouring sites relative to the '**A**' sub-lattice. Using equation (1.2), we

The Electronic Band structure of Graphene
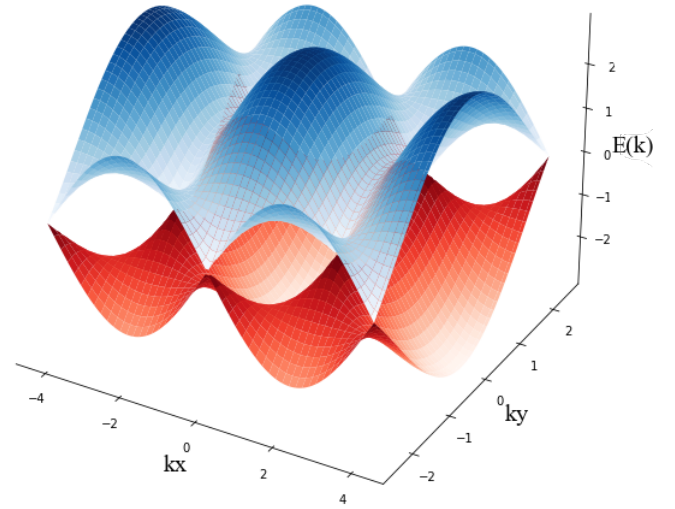
Figure 1.3. The electronic band structure of monolayer graphene generated in python (see appendix iv.) using eq. 1.34. and nearest neighbour parameters (eq. 1.2). The π and π^*-bands converge at the six Dirac points (K and K' points) which lies at the Fermi level ($E_\pm(k) = 0$). These points bound the hexagonal structure in momentum space referred to as the Brillouin zone

have an adequate substitution for each $R_{B,l} - R_{A,i}$ term, namely the relative δ_l terms.

$$H_{A,B} = -\gamma_0 f(k), \quad f(k) = \sum_{l=1}^{3} e^{ik(R_{B,l}-R_{A,i})} \tag{1.30}$$

Equivalently, the opposing off-diagonal term is just the complex conjugate of H_{AB} [31].

$$H_{A,B} \approx -\gamma_0 f(k), \quad H_{B,A} \approx -\gamma_0 f^*(k) \tag{1.31}$$

Expanding $f(k)$ using (1.2):

$$f(k) = e^{i\left(-\frac{a}{2}kx+\frac{\sqrt{3}a}{2}ky\right)} + e^{i\left(-\frac{a}{2}kx+\frac{-\sqrt{3}a}{2}ky\right)} + e^{iakx}$$

$$= e^{iakx} + e^{-i\frac{a}{2}kx}\left(e^{i\frac{\sqrt{3}a}{2}ky} + e^{i\frac{-\sqrt{3}a}{2}ky}\right)$$

$$= e^{iakx} + 2cos(\frac{\sqrt{3}a}{2}ky)e^{-i\frac{a}{2}kx} \tag{1.32}$$

2.2.6   The Electronic Band Structure near Fermi level

All necessary ingredients for constructing the secular equation (1.24) have been achieved, and in turn, graphenes electronic band structure at low energy levels can be obtained:

$$H\psi_j = E_j\psi_j$$

$$\begin{pmatrix} \varepsilon_{2p} & -\gamma_0 f(k) \\ -\gamma_0 f*(k) & \varepsilon_{2p} \end{pmatrix}\begin{pmatrix} \psi_{jl} \\ \psi_{jl+1} \end{pmatrix} = E_j\begin{pmatrix} \psi_{jl} \\ \psi_{jl+1} \end{pmatrix} \tag{1.33}$$

Now forming the explicit determinant seen in (1.24). setting = 0 and solving yields the eigen-pair solutions for the tight-binding Hamiltonian:

$$det\begin{pmatrix} 0-E & -\gamma_0 f(k) \\ -\gamma_0 f*(k) & 0-E \end{pmatrix} = 0 \tag{1.34}$$

Therefore, The energy bands are given by:

$$E(k) = \pm\gamma_0\sqrt{1+4cos^2\left(\frac{\sqrt{3}a}{2}k_y\right)+4cos\left(\frac{3a}{2}k_x\right)cos\left(\frac{\sqrt{3}a}{2}k_y\right)} \tag{1.35}$$

Equation (1.35) above forms two bands, namely the conduction ($E_-(k)$) and valence $E_+(k)$) bands, which coalesce at the six Dirac points **K** and **K'** at the Fermi level. This can be seen previously in **figure 1.3** which displays graphenes electronic band structure in momentum space, confined to the first Brillouin zone. Graphene's electronic band structure contains some very unique and potentially exotic properties. Firstly, the plot (1.3.) describes the Energy dispersion as a function of the in plane x and y crystal momentum $E(k)$, namely, $\mathbf{k_x}$ and $\mathbf{k_y}$. The convergence of the bands at the **K** and **K'** points alludes to graphenes gap-less band-structure, making graphene a semi-metal [19][20][46]. Near these points, the bands structure resembles a conical structure ("Dirac cones") and the energy dispersion regime is linear, and the dynamics of the charge carriers attribute speeds of $\approx 0.003c$,thus become "quasi-relativistic" which can be described by an effective two-dimensional Dirac like Hamiltonian [10][31]. An important distinction should be made for the correspondence between the Dirac points and the relative **K** and **K'** points. Thusfar, both have been treated on equal footing, however in the context of strained systems, where we have varying hopping parameters along the δ_1, δ_2 and δ_3 vectors, the Dirac points can drift away from their crystallographic **K** and **K'** symmetry points. To be more explicit, the Dirac point correspond to the point of convergence between the π and π^*-bands [19]. The emergence of these effectively "massless" 2D fermions will become clear in the next section when the expressions for $f(k)$ is expanded about the **K** and **K'** points for approximately low energy dispersion of $< |\gamma_0|$.

2.2.7   The Density of States of Graphene

Determination of the eigen-values (1.35) corresponding to the band structure makes for a rather trivial extraction of the density of states (DOS) in graphene. In the very general case, the DOS can be computed by taking a two dimensional integral over the Brillouin zone and summing over the eigen-values corresponding to the upper and lower bands :

$$\rho(E) = -\frac{1}{\pi}\lim_{\eta\to 0}\text{Im}\left\{\sum_\zeta\frac{1}{\Omega_{BZ}}\int_{BZ}\frac{dq_x dq_y}{E-E_q^\zeta+i\eta}\right\}$$

$$\sum_\zeta\frac{1}{\Omega_{BZ}}\int_{BZ}\delta(E-E_q^\zeta)\,dq_x dq_y \qquad (1.36)$$

In this case the Normalisation coefficient corresponds to the number of states per unit cell. However, this can be rather involved, and a simplification can be constructed by:

$$\rho(E) = \frac{1}{N}\sum_{i=1}^n\delta(E-\lambda_i) \qquad (1.37)$$

Which contains the normalisation coefficient $\frac{1}{N}$, whereby "N" corresponds to the quantity of atoms present. The entirety of the electronic bandwidth is considered "E"; and a summation over every λ_i term is executed, which corresponds to each "ith" eigenvalue. Moreover, the Dirac delta function $\delta(E-\lambda_i)$ now can be approximated by the Lorentzian distribution:

$$L_\lambda(E) = \frac{1}{\pi}\frac{\frac{1}{2}\Gamma}{(E-\lambda_i)^2+(\frac{1}{2}\Gamma)^2} \qquad (1.38)$$

Therefore, the DOS takes the approximate form:

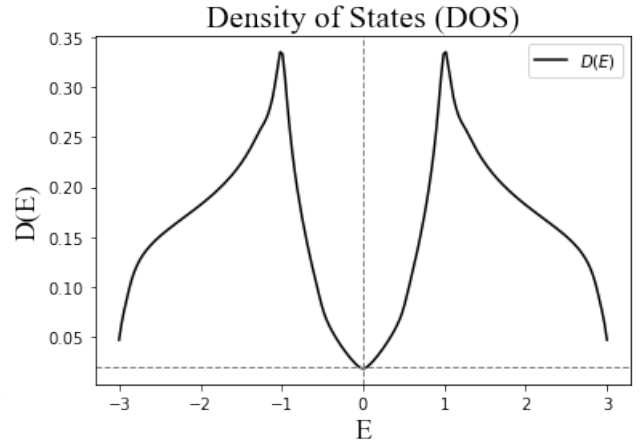$$\rho(E) = \frac{1}{N}\sum_{i=1}^n L_\lambda(E) \qquad (1.39)$$

Figure 1.4. The DOS of graphene generated using the "semi-infinite" model in python (see appendix iii.) Using $\Gamma = 10^{-2}$ N = 100 (25 x 25) system. The discrepancy in the convergence to zero in the vicinity of the charge neutrality point (Dirac point), between the semi-infinite and the finite model is contrasted in section 3.1.1

The Γ term corresponds to the "Broadening factor", or width of the Lorentzian curve. The curve centres about each of the points λ_i as i $\to$ n. Figure 1.4 below demonstrates the Density of states for graphene.

Typically, in the infinite idealised case, the linear convergence of the DOS goes to zero at the charge neutrality point (Dirac Point), which is a unique property of graphene. This property differs significantly from the conventional 2D parabolic systems, where the DOS remains constant [45]. This can be further seen in the continuum limit in figure 1.4. The presence of "Van Hove singularities" occurs at points where $\rho(E)$ becomes non differentiable, which correlate to the critical points (saddle-points) of the energy at the edge points **M** (see fig 1.2.) of the Brillouin zone.

2.3   The Continuum model for 2D massless Dirac Fermions

The implications of QED intrinsic to graphene's low energy dispersion regime is a direct consequence to the geometry of the Fermi surface about the Dirac points. The conical dispersion in momentum-space implies the existence of 2D effectively massless Dirac fermions, which can be described the 2D Dirac like Hamiltonian, whose solutions demonstrate the linearity relation between the energy and momentum of the charge carries [45][48]. This very pertinent link to QED has a plethora of consequences, however most relevant to this project is the emergence of strain induced pseudo-gauge fields; and how their properties emerge within the continuum description of graphene, giving rise to substantial pseudo-magnetic fields (see.)[34-36].

2.3.1   The 2D Mass-less Dirac Hamiltonian

To construct to Dirac-like Hamiltonian, the eigen-spectrum (1.30) is expanded about the immediate vicinity of the **K** and **K'** points. Beginning with the **K** point, a relative 2D momentum vector is defined; $q = \mathbf{k} - \mathbf{K}$. (differing by a factor of) Equation (1.30) is written in terms of q, by substitution and expanding around $q = 0$[31][45]:

$$f(\mathbf{K+q}) = \gamma_0\left[e^{ia\mathbf{K_x}}e^{ia\mathbf{q_x}}+2cos\left(\frac{\sqrt{3}a}{2}(\mathbf{K_y+q_y})\right)e^{i-\frac{a}{2}\mathbf{K_x}}e^{i-\frac{a}{2}\mathbf{q_x}}\right] \qquad (1.40)$$

$$f(\mathbf{K+q}) \approx -ie^{-i\mathbf{K_x}a}\frac{3a\gamma_0}{2}(\mathbf{q_x}+i\mathbf{q_y}) \qquad (1.41)$$

The phase factor $-ie^{-i\mathbf{K_x}a}$ can be omitted, and infact the term $\frac{3a\gamma_0}{2} = \mathbf{v_F}$, the Fermi velocity, which is $\approx 0.003c$. Finally, reintroducing :

$$f(\mathbf{q})_\mathbf{K} \approx \mathbf{v_F}(q_x + iq_y) \qquad (1.42)$$

Similarly, identical methodology is conducted for expansion about the K' point with just a simple change of helicity[31][43-45]. Therefore:

$$f(\mathbf{q})_{\mathbf{K}'} \approx \mathbf{v_F}(q_x - iq_y) \qquad (1.43)$$

Expressions (1.38) and (1.39) can effectively be substituted into the expression for the tight-binding model, replacing the previous off diagonal elements, forming the Dirac Hamiltonian:

$$H = \begin{pmatrix} 0 & (\mathbf{q_x} + i\mathbf{q_y}) \\ (\mathbf{q_x} - i\mathbf{q_y}) & 0 \end{pmatrix} \qquad (1.44)$$

Using the Pauli matrices $\boldsymbol{\sigma} = \sigma_x, \sigma_i$, we can express this simply as:

$$H(q) = \mathbf{v_F}\boldsymbol{\sigma}|\mathbf{q}| \qquad (1.45)$$

$$E_\pm(q) \pm \mathbf{v_F}|\mathbf{q}|, \quad \psi_{\mathbf{K}_\pm}(\mathbf{q}) = \frac{1}{\sqrt{2}}\begin{pmatrix} e^{i\frac{\theta_\mathbf{q}}{2}} \\ \pm e^{-\frac{\theta_\mathbf{q}}{2}} \end{pmatrix},$$

$$\theta_\mathbf{q} = tan^{-1}\left(\frac{\mathbf{q_x}}{\mathbf{q_y}}\right) \qquad (1.46)$$

Where E($\mathbf{q}$) and $\psi_{\mathbf{K}_\pm}(\mathbf{q})$ correspond to the eigen-values, and eigen-functions of the Dirac Hamiltonian respectively, The eigen-values clearly represent linear dispersion regime for effectively massless fermionic particles. Figure 1.5 below displays the linearity of the dispersion corresponding to the Valence (E_+) and Conduction (E_-) bands in momentum space. The eigen-functions can be described by a Dirac-like spinor structure whose properties are similar to the spinor structure used to describe fermionic particles in 1 + 3 dimensional space in QED. However, there are some fundamental distinctions between the Spinors formed in the context of condensed-matter physics with those in QED. Firstly, the emergence of negative energy states in the solutions of the Dirac equation in context of QED indicates perhaps the existence of particle/anti-particle pairs, which isn't exactly the case in condensed-matter physics. The positive and negative solutions correspond to the valley index of the electron-hole pair formed in about the Dirac points in the conduction and valence bands. The manifestation of an additional degree of freedom referred to as "Pseudo-spin", which plays the role of real spin, primarily emerges due to the existence of the valley indices and the non-equivalent Dirac points in the band structure. Moreover, Implicit in (1.42) is the coupling between the pseudo-spin and the $\mathbf{q}$-vector, therefore, fermions corresponding to the upper Dirac cone on the $\mathbf{K}$ point $\rightarrow \mathbf{E}_+(\mathbf{q})$, have a s = +1 (effective spin-up) state , which are parallel with the direction of propagation. Conversely, the lower cone is reversed and has s = -1 (effective spin-down) state. The helicity is ultimately changed for the corresponding $\mathbf{K}'$ point, giving rise to graphene's chiral like property. [47]
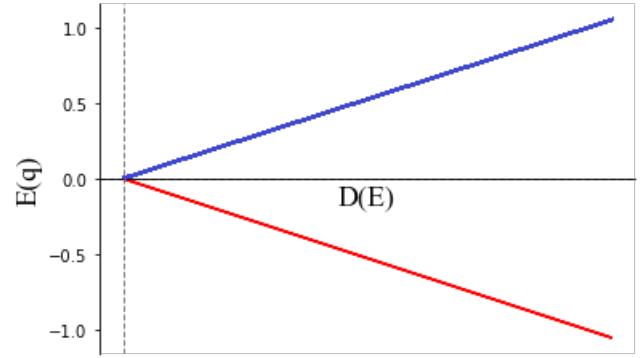
Linear Dispersion Regime of Graphene

Figure 1.5. The Linear dispersion regime E(q) for monolayer graphene generated in python (see Appendix iv.) confined to the first order in $|\mathbf{q}|$. The $\mathbf{K}$ (E_+) and $\mathbf{K}'$ (E_-) bands converge at the Dirac point.

2.4   Strain Induced Gauge Fields and Pseudo-Magnetic Fields

The manifestation of effective-gauge fields as a consequence of geometric lattice strain once again provides for an analogous coupling between condensed matter physics and QED. In the low energy Dirac regime, lattice deformations lead to perturbations of the Dirac equation in the form of an effective gauge field **A** [34-35][49-51]. The emergence of the gauge field is coupled to the spatial dependency of the new modulated hopping integral matrix element $\gamma_{\mathbf{ij}}$. In conjunction with the effective-gauge field description associated with the hopping term disparities, there also emerges an effective scalar field ϕ due to the relative change in local charge distribution [34-35][50]. The effective gauge field can be equivocated to the vector potential description in classical electrodynamics [35]. Therefore the relations $\mathbf{E} = -(\nabla\phi + \partial_t\mathbf{A})$ and $\mathbf{B} = \nabla \times \mathbf{A}$ indeed provide for suitable descriptions, implicit of which are the existence of pseudo-magnetic fields (PMFs) due to the spatial dependency of the effective gauge field. The distinction between PMFs and real magnetic fields, as alluded to earlier regards the preservation of time reversal symmetry. This becomes obvious in the Dirac Hamiltonian expression as the gauge field **A** takes opposing signs in each of the off-diagonal components, corresponding to each in-equivalent sub-lattice point such that $\mathbf{A_K} = -\mathbf{A_{K'}}$. The implications of time reversal symmetry conservation implies a degeneracy in eigen-values corresponding to the **k** and **-k** wave-vectors in the upper and lower bands as each are related under the time reversal transformation $T : t \rightarrow -t$ such that the eigen-states $T\psi(r,t) = \psi^*(r,-t)$.

2.4.1   Strain modulated Nearest Neighbour Tight-Binding Parameters

The imposition of geometric lattice strain subsequently affects the carbon-carbon bond length between neighbouring atomic sites. As a consequence of this, graphene's unit cell becomes distorted and the pristine electronic characteristics no longer provide for a full description of the electronic properties of the system. The effects of strain can be described by the continuum elasticity model, provided the magnitude of the strain is confined to the limits of continuum mechanics. In this context, the strain can be described effectively the rank 2 strain tensor. The strain tensor takes the explicit form [50]:

$$\varepsilon_{ij} = \frac{1}{2}(\partial_j u_i + \partial_i u_j + \partial_i h \partial_j h)$$

9

$$= \begin{bmatrix} \varepsilon_{xx} & \varepsilon_{xy} & \varepsilon_{xz} \\ \varepsilon_{yx} & \varepsilon_{yy} & \varepsilon_{yz} \\ \varepsilon_{zx} & \varepsilon_{zy} & \varepsilon_{zz} \end{bmatrix}$$

$$= \begin{bmatrix} \partial_x u_x + \partial_x h \partial_x h & \frac{1}{2}(\partial_y u_x + \partial_x u_y + \partial_x h \partial_y h) \\ \frac{1}{2}(\partial_x u_y + \partial_y u_x + \partial_y h \partial_x h) & \partial_y u_y + \partial_y h \partial_y h \\ \frac{1}{2}(\partial_x u_z + \partial_z u_x + \partial_z h \partial_x h) & \frac{1}{2}(\partial_y u_z + \partial_z u_y + \partial_z h \partial_y h) \end{bmatrix}$$

$$\begin{bmatrix} \frac{1}{2}(\partial_z u_x + \partial_x u_z + \partial_x h \partial_z h) \\ \frac{1}{2}(\partial_z u_y + \partial_y u_z + \partial_y h \partial_z h) \\ \partial_z u_z + \partial_z h \partial_z h \end{bmatrix} \tag{1.47}$$

However, the geometry that concerns out of plane displacements can be parameterised by the projection of the curved surface $h = h(x,y)$ onto a flat Euclidean surface. The in-plane displacement components of the strain tensor are considered negligible and are sufficiently omitted [49-51]. Therefore, the (1.47) reduces to only the ε_{xx}, ε_{xy} and ε_{yy} out of plane components ($\varepsilon_{xy} = \varepsilon_{yx} \to 2\varepsilon_{xy}$:

$$\varepsilon_{ij} = \frac{1}{2}(\partial_i h \partial_j h) \tag{1.48}$$

The implications of imposing strain parameterised by some function $h = h(x,y)$ onto graphene's lattice structure ultimately changes the carbon-carbon bond length of neighbouring sub-lattice points and consequently modifies the characteristics of the NNTB Hamiltonian. More precisely, the hopping integral matrix element in idealised graphene, which is characterised by a scalar quantity $\gamma_0 \approx -2.8eV$ [18][50], now becomes a spatially dependent function parameterised on the relative displacement of neighbouring atoms $\gamma_{ij} = \gamma(\delta_i, \delta_j)$. Whereby the displacement vectors δ_i' are defined by $\delta_i' = \delta_i + u$, where δ_i is the bond length vector at equilibrium and u correponds to the relative displacements. The new modified bond length $|\delta_{ij}'|$ can be determined from the strain tensor (1.48) [49][52]

$$|\delta_{ij}'| \approx a_0 + \frac{1}{a_0} \delta_{ij} \cdot \varepsilon_{ij} \cdot \delta_{ij}$$

$$= \frac{1}{a_0}(a_0^2 + \varepsilon_{xx}x_{ij}^2 + \varepsilon_{yy}y_{ij}^2 + 2\varepsilon_{xy}x_{ij}y_{ij}) \tag{1.49}$$

where a_0 is the unperturbed carbon-carbon bond length between sites $\approx 1.42\text{Å}$. The new modulated hopping term γ_{ij} can now be formulated using the expression seen in (1.49) [18].

$$\gamma_{ij} = \gamma_0 e^{-\beta\left(\frac{|\delta_{ij}'|}{a_0} - 1\right)} \tag{1.50}$$

Whereby the coefficient term $\beta = |\frac{\partial log \gamma_0}{\partial log a_0}| \approx 3.37eV$ achieved empirically from [53]. The magnitude of the hopping energy decreases exponentially relative to the increase in displacement between neighbouring sub-lattice points, and its form obtained a priori [18][54]. The new modulated hopping term γ_{ij} serves as a direct substitution for γ_0 in the NNTB Hamiltonian. Therefore, the new modulated Hamiltonian differs by the substitution $\gamma_0 \to \gamma_{ij}$. In context of the finite method, the Hamiltonian can be expressed compactly using projection operations once again:

$$H = \sum_i |i\rangle \varepsilon_i \langle i| + \sum_{\langle i,j \rangle} |j\rangle \gamma_{ij} \langle j| \tag{1.51(a)}$$

Where ε_i corresponds to the onsite energy located at sub-lattice site "i", and γ_{ij} is the corresponding new modulated hopping integral.

Similarly, for the Hamiltonian using the Bloch formulation we conduct the same substitution $\gamma_0 \to \gamma_{ij}$, therefore:

$$H = \begin{pmatrix} 0 & -\gamma_{ij}f(k) \\ -\gamma_{ij}f^*(k) & 0 \end{pmatrix} \tag{1.51(b)}$$

Where ε is set to zero.

2.4.2   Emergent Gauge fields and Pseudo-magnetic fields in the continuum model

The presence of out of plane, smooth lattice deformations characterised by (1.48) induces deformations of the bond lengths described by (1.49) which subsequently yields a spatially dependant hopping parameter as seen in (1.50). Considering the hopping integral $\gamma_0 \approx -2.8eV$ is a constant value in pristine graphene (as the inter-atomic distances are considered to be in equilibrium), the introduction of a spatially varying hopping term such that $\gamma_{ij}(\delta_i, \delta_j) = \gamma_0 + \Delta\gamma_{ij}(\delta_i, \delta_j)$ implies a small perturbation $\Delta\gamma_{ij}$ in the equilibrium length, which amends a small correction term to the Dirac Hamiltonian in the form of an effective gauge field **A** [55-56]. The redistribution of electron density due to strain also emends a scalar potential term ϕ to the Dirac Hamiltonian. The PMF quantities emerge by virtue of the relation $\mathbf{B} = \nabla \times \mathbf{A}$. Following [55] p.22, the effective gauge field can be achieved: Consider some strain characterised by a smooth function onto a planar sheet of graphene, the vector potential **A** can be decomposed into $\mathbf{A} = A_x e_x + a_y e_y$ where $[e_x, e_y]$ form an orthogonal basis in which e_x is adjacent to the "zig-zag" direction and e_y to the "armchair" direction. The effective gaue field is related to the perturbation $\Delta\gamma_{ij}$ by the following [57]:

$$A_x(r) - iA_y(r) \equiv -\frac{1}{ev_F} \sum_{i,j}^n \Delta\gamma(r_i, r_j)e^{i\mathbf{K}\cdot\delta_{ij}} \tag{1.52}$$

Using the expression: $\gamma_{ij}(\delta_i, \delta_j) = \gamma_0 + \Delta\gamma_{ij}(\delta_i, \delta_j)$ and expanding γ to first order of the strain tensor:

$$\gamma_{ij} \approx \gamma_0 \left(1 - \frac{\beta}{a_0^2} \delta_{ij} \cdot \varepsilon_{ij} \cdot \delta_{ij}\right) \tag{1.53}$$

Substituting this expression into (1.52) yields the expression for the effective gauge field:

$$\mathbf{A} = -\frac{\beta}{2ea_0} \begin{pmatrix} \varepsilon_{xx} - \varepsilon_{yy} \\ -2\varepsilon_{xy} \end{pmatrix} \tag{1.54}$$

Therefore the effective Dirac Hamiltonian (1.44) takes the modulated form:

$$H = \begin{pmatrix} 0 & (\mathbf{q_x} + i\mathbf{q_y} \pm e\mathbf{A}) \\ \mathbf{q_x} - i\mathbf{q_y} \pm e\mathbf{A} & 0 \end{pmatrix} \tag{1.55}$$

$$H(\mathbf{q})_{K,K'} = v_F \sigma \cdot (\mathbf{q} \pm e\mathbf{A}) \tag{1.56}$$

Its important to note the distinction between the signs for each component. By convention the **K** valley corresponds to $+e\mathbf{A}$ for the first off diagonal entry and $-e\mathbf{A}$ for the remaining. Conversely, and implicit in which is the preservation of time-reversal symmetry, is the change of helicity between **K** and **K'**, therefore the first off diagonal entry and $-e\mathbf{A}$ and $+e\mathbf{A}$ for the remaining. Moreover, the inclusion of the scalar potential term implies the effective Dirac Hamiltonian takes the form [50] :

$$H(\mathbf{q})_{K,K'} = v_F \sigma \cdot (\mathbf{q} \pm e\mathbf{A}) + \phi(r)\sigma_0 \tag{1.57}$$
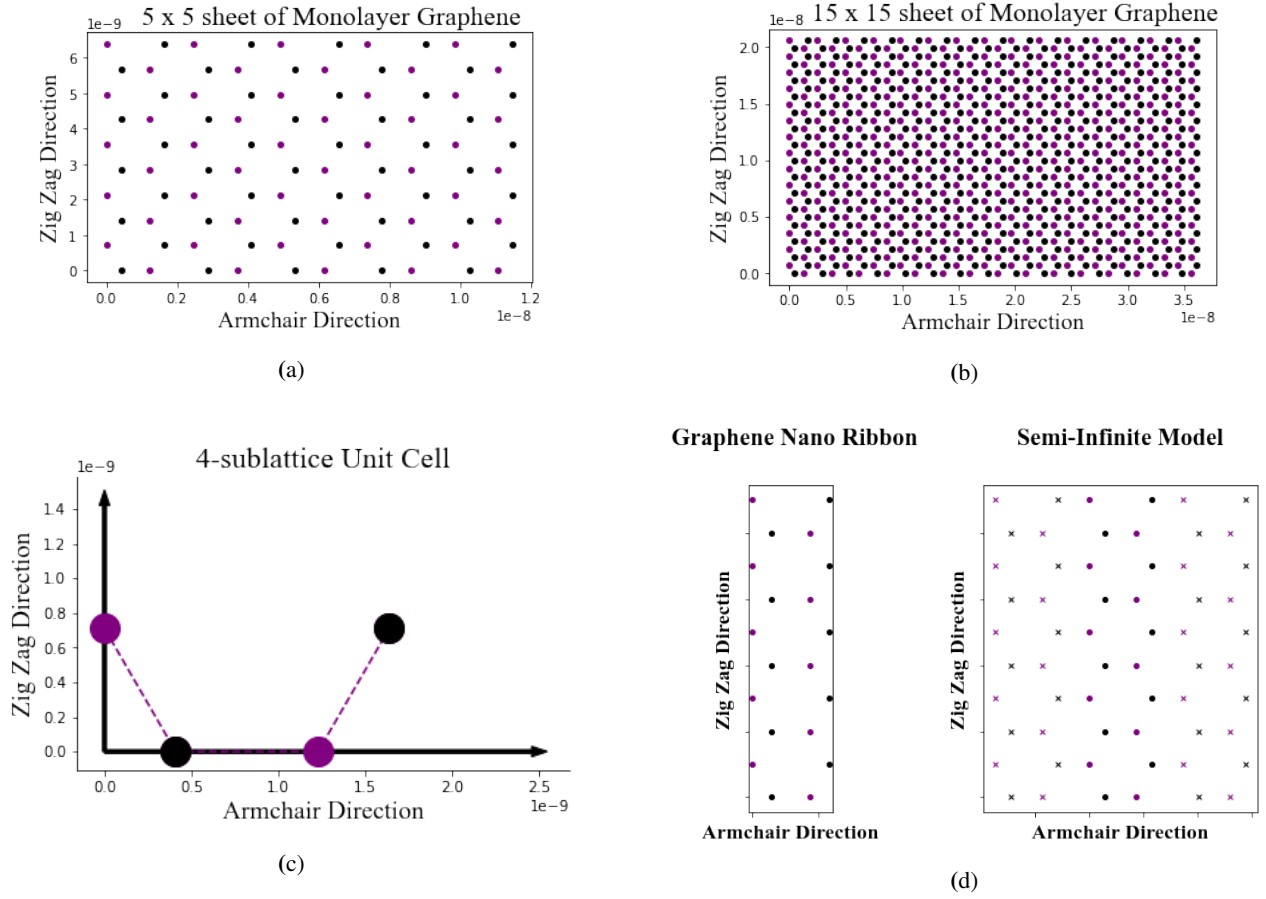
(a)

(b)

(c)

(d)

Figure 1.6 (a) Corresponds to a 5 x 5 Unit cell sheet of monolayer graphene. This was generated in python utilising the methodology outlined above (see appendix ii.). The sheet consists of 100 carbon atoms in total, 20% of which are "zig-zag" edge states. **(b)** Corresponds to a 15 x 15 Unit cell sheet of monolayer graphene. The sheet consists of 900 carbon atoms in total, $\approx 6\%$ or which are "zig-zag" edge states. **(c)** 4-sublattice unit cell implementation for graphene, which constitutes of points {**A**, **B**, **A'**, **B'**} where **A**, **A'** = purple and **B**, **B'** = black. the carbon-carbon bond length = a = 1.42Å. **(d)** The graphene nano ribbon (left), in this context $n_x = 1, n_y = 5$. and the attachment of the artificial cells (right) labelled by the marker "x".

Where the scalar potential term: $\phi(r) = g_s(\varepsilon_{xx} + \varepsilon_{yy})$, $g_s \approx -2eV$ and σ_0 corresponds to a 2 x 2 identity matrix [35][50]. Finally, as mentioned previously, the spatially dependent effective gauge field implies for the existence of a pseudo-magnetic field through the relation:

$$B_p = \nabla \times \mathbf{A} \equiv \partial_x A_y - \partial_y A_x \qquad (1.58)$$

The continuum model provides for the analysis of strain about the low energy Dirac points, and therefore is typically used to discuss the emergence of the pseudo gauge and magnetic fields. Description of the electronic properties pertinent to the system as a whole is confined to the NNTB model calculations.

3 Implementation and Analysis

As a brief overview, all procedures outlined were implemented in Jupyter Notebook python v.3.8.8. The procedures outlined below are posed chronologically. Beginning with the construction of the real space graphene unit cell lattice structure, its implementation is generalised such that one can form an arbitrarily large n x n plane of consecutive graphene unit cells, or more commonly, monolayer graphene. Rudimentary electronic properties, such as the band structure, energy spectrum and DOS are extracted and discussed from the pristine model via the finite and semi-infinite NNTB calculations. The monolayer sheet simulations provides for a basis to impose geometric strain. In particular strain characterised by the Monge representation [50] is considered, such that we have a one to one mapping between a curved surface and a flat Euclidean plane. The strain function is parameterised by h = h(x,y), where h(x,y) is a smooth and continuous function. Strain geometries investigated include Gaussian folds, Bubbles and ripples. The implications of the strain profiles are discussed initially via the continuum Dirac model, in which the emergent pseudo-gauge and pseudo-magnetic fields corresponding to the strain geometries are demonstrated as a consequence of the spatial dependencies in the integral hopping matrix elements. The physical implications of these emergent fields are discussed in regards to their effect on Graphene's intrinsic electronic properties and compared with results found in literature. The emergence of "snake-state" become apparent in regions of changing pseudo-magnetic field signs, at the extremities of the geometries. The snake states are qualitatively discussed in context of nano-wire and wave-guiding mechanisms. Nano-ribbons are utilised in the semi-infinite model to characterise the effects of certain strain geometries on the Graphene's electronic properties such as its band structure and DOS. The probability densities are evaluated for specific states confined within the strain region Moreover out of plane strain has demonstrated to shift the location of the Dirac points from their symmetric crystallographic **K** and **K'** points.
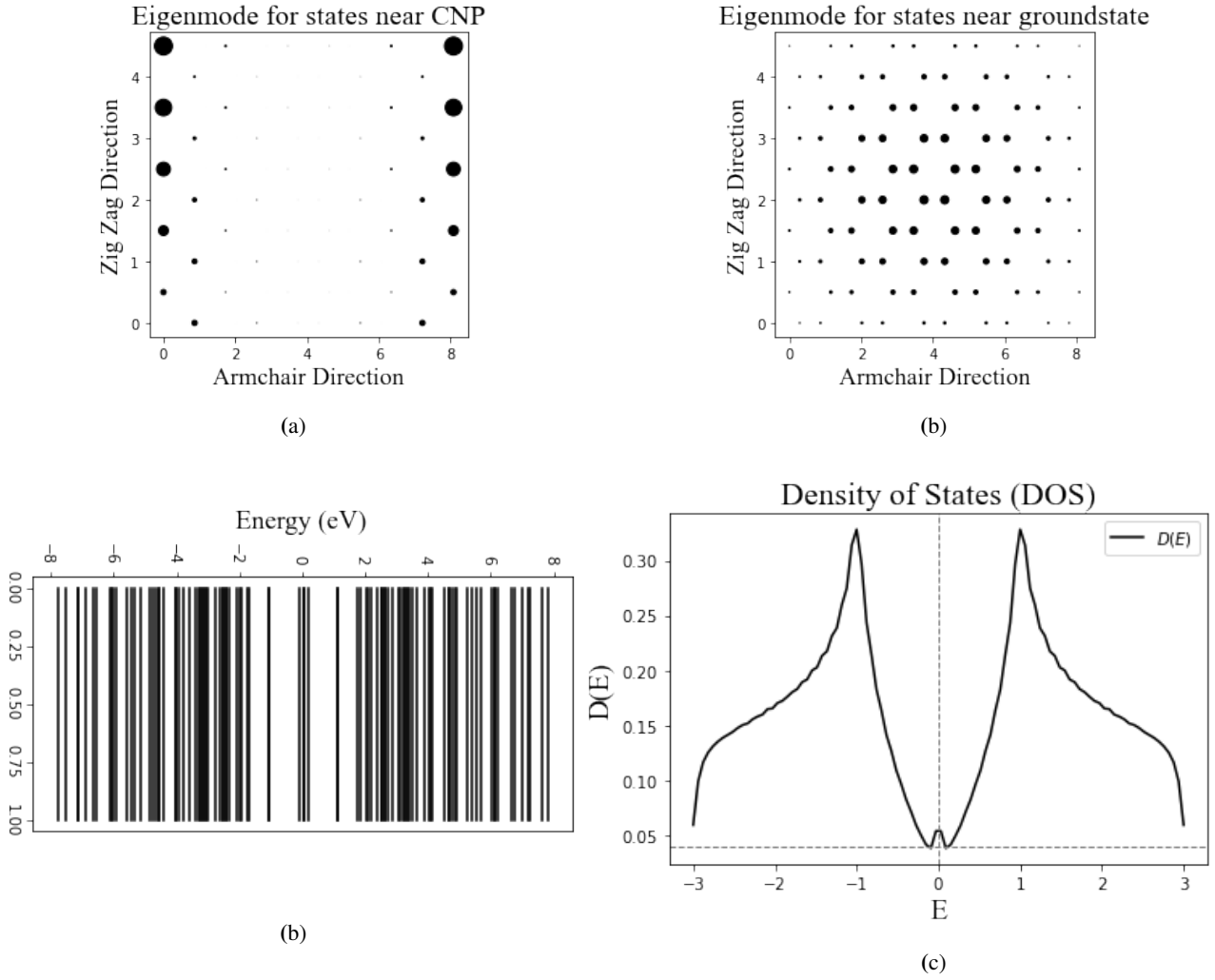
11

(a)

(b)

(b)

(c)

Figure 1.7 (a) Corresponds to the eigen-mode for the states that exist near the half filling of the band structure (Zig-Zag edge states) for n = 50/100 atoms in contrast to the eigen-mode for states near the ground-state, n = 0/100. **(b)** The eigen-value spectrum calculated for a finite (15 x 15) sheet of monolayer graphene ranging from in $\approx -8 - 8eV$ **(c)** The DOS corresponding to the finite system, which can be contrasted with the semi-infinite system (1.4)(1.7(b)). Notice the absence of complete convergence to zero at the charge neutrality point, due to the existence of edge states.

3.1   Simulating the Real Space Pristine Lattice Structure

To construct graphenes unit cell, the discrete translational vectors associated with the Bravais lattice, outlined in section 2.1.2, namely $\mathbf{R_a} = n_1\mathbf{a_1} + n_2\mathbf{a_2}$ and similarly, $\mathbf{R_b} = n_1\mathbf{b_1} + n_2\mathbf{b_2}$, which map successive A and B Sub-lattice points are omitted. Instead, a non-primitive unit cell is constructed, composed of four sub-lattice points {A, B, A', B'}, although conventionally one would assume these are two sets of two in-equivalent A and B points, however, in the context of purely implementation, the formerly equivalent points cannot be mapped through a vector transformation. (Its true that infact A and A' are still physically equivalent). Figure 1.6 demonstrates the unit cell, where the set of points {A, B, A', B'} are relative to an orthogonal basis $e_x \cdot e_y = 0$ with the "zig-zag" direction orientated in the e_y direction and the corresponding "armchair" direction orientated along e_x.

The initial set of four sub-lattice points can be expanded on the basis such that:

they can be described in terms of their components:

$$\mathbf{A} = \frac{a}{2}e_y \quad \mathbf{B} = \frac{a}{2\sqrt{3}}e_x$$

$$\mathbf{A'} = \frac{a\sqrt{3}}{2}e_x \quad \mathbf{B'} = \frac{2a}{\sqrt{3}}e_x + \frac{a}{2}e_y \tag{2}$$

The linear map $f : \mathbb{R}^2 \to \mathbb{R}^2$ where $f(x,y) = (X_i + a_1n_x, Y_i + a_2n_y)$ describes the mapping function to any nth point, such that the points can be expanded into a $n_x \times n_y$ monolayer sheet of graphene unit cells, where $n_x, n_y \in \mathbb{N}$. The X_i term regards the position of sub-lattice point along e_x where $i \in \{A, B, A', B'\}$ and similarly for Y_i, with the exception of its position corresponding to e_y. The a_1 and a_2 terms are scaling factors where $a_1 = \sqrt{3}a$ and $a_2 = a$. More explicitly, regarding implementation, two numerical arrays each composed of x and y values are configured with their respective initial entries corresponding to (2). The function which maps each corresponding sub-lattice point to its nth point consists of a nested for loop with lengths equivalent to n_x and n_y respectively. For every iteration, each sub-lattice point is scaled from its original position to its corresponding n_x and n_yth point.

i. The Finite Model of Monolayer Graphene

Figure 1.6 (a) and (b) demonstrates a (5 x 5) sheet of monolayer graphene i.e $n_x = 5$ and $n_y = 5$ and a (15 x 15) sheet, $n_x = 15$ and $n_x = 15$ respectively. Each were achieved by the methods outlined previously. Both planes of which are scaled

Electronic Bandstructure of Graphene
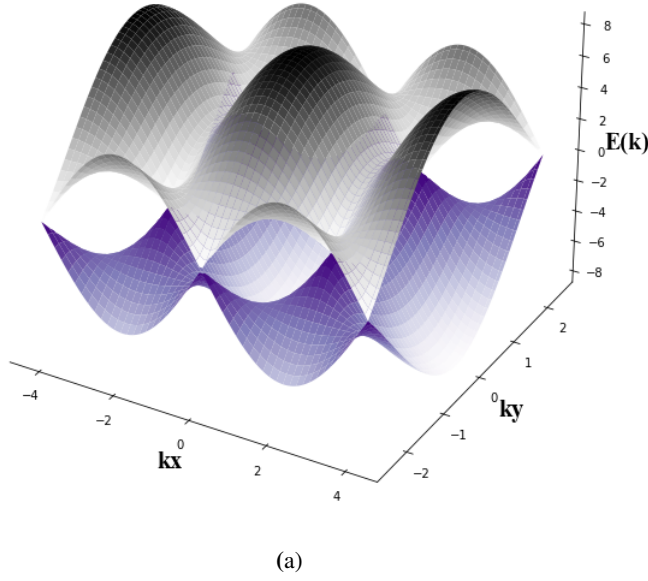
Band Structure: Dirac Point

(a)

(b)
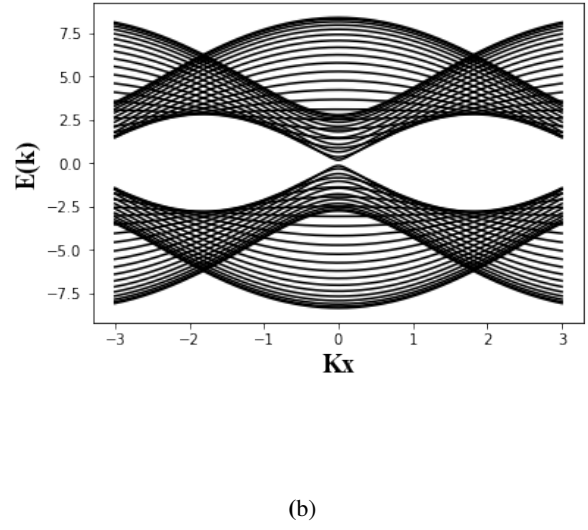
Figure 1.8 (a) Graphene's electronic band structure displayed in three-dimensions in the vicinity of the first Brillouin zone in momentum-space. The conduction and valence bands touch at the charge neutrality points (Dirac points). The dispersion $E(k)$ about these points is linear and gives rise to the "quasi-relativistic" fermions. **(b)** The band structure projected in two-dimensions, computed using the semi-infinite model for $n_y = 25$.

accordingly to the carbon-carbon distance, a = 1.42Å. The finite Hamiltonian (2.1) was applied to the case of the 5 x 5 to demonstrate the spatial distribution of energy states in finite systems. This provided for the necessary comparison, to a more accurate prediction achieved by the semi-infinite model. Comparatively, the distribution of energy states in the semi-infinite model of pristine graphene will of course be homogeneous and isotropic as the edge states no longer exist , thus extracting information about its electronic properties will not be affected by such.

ii. The Semi-infinite Model of Monolayer Graphene via Nano Ribbons

The construction of these n_x x n_y monolayer sheets provides a sufficient basis for the analysis of geometric strain in context of observing the qualitative effects from the emergent pseudo-gauge and pseudo-magnetic fields in the continuum model (see section 3.3). Although it is possible to extract useful information about graphenes electronic properties from a finite sheet of graphene, more accurate depictions are produced by the construction of an effectively semi-infinite model. This particular model can be constructed by the creation of a nano-ribbon, which has dimensions of width equivalent to a single unit cell i.e, $n_x = 1$ and its length can be arbitrarily long such that $n_y \to \infty$. Each side of the nano-ribbon is connected to "artificial" unit cells of equivalent dimensions. The addition of these cells provides for a way to determine the nearest-neighbour hopping terms between neighbouring sites. Figure 1.6 (d) demonstrates this methodology. The "x" markers correspond to the artificial cells. Considering the nano-ribbon is effectively infinite along e_y, this particular method allows for the analysis of certain strain geometries which are invariant in the x-direction only. This method also provides for an accurate extraction of the electronic band structure, for which the subsequent effects of

strain geometries can be contrasted.

3.1.1   Electronic Properties of Pristine graphene

i. The Finite Hamiltonian

For finite monolayer graphene sheets, such as those outlined in figure 1.6 (a) and (b), the generic energy spectrum corresponding to the real space Hamiltonian can be achieved by solving the eigen-value problem for the Hamiltonian below:

$$H = \sum_i |i\rangle \varepsilon_i \langle i| + \sum_{\langle i,j \rangle} |j\rangle \gamma_{ij} \langle j| \qquad (2.1)$$

Which corresponds explicitly to :

$$H = \begin{bmatrix} \varepsilon_1 & \gamma & 0 & \gamma & 0 \\ \gamma & \varepsilon_2 & \cdots & & \gamma \\ 0 & \cdots & \cdots & \cdots & \vdots \\ \gamma & \cdots & \cdots & \varepsilon_{n-1} & \gamma \\ 0 & \gamma & 0 & \gamma & \varepsilon_n \end{bmatrix} \qquad (2.1)$$

Where the diagonal elements, ε_n corresponds to the onsite energy, and its projection $|i\rangle \varepsilon_n \langle i|$ onto orbital site "i". The off diagonal terms $\gamma \approx -2.8eV$ are the hopping integral matrix elements which remain constant in pristine graphene [21-30]. The projection operator $|j\rangle \gamma_{ij} \langle j|$ is confined to the nearest neighbouring sites only. Figure 1.10 below corresponds to the eigen-value and eigen-mode spectrum for the case of a finite 5 x 5 monolayer graphene sheet. (see appendix ii.) for the explicit numerical Hamiltonian matrix, and solutions). Figure 1.7(a) is achieved under several imperative assumptions, firstly, each of the onsite energies ε_i associated with the p_z orbitals are all equivalent, such that $\varepsilon_i = \varepsilon_{i+1} = 0.02eV$. Due to the homogeneity of this factor, the factor sets the scale of the charge neutrality point, and in most cases it can be omitted [31].
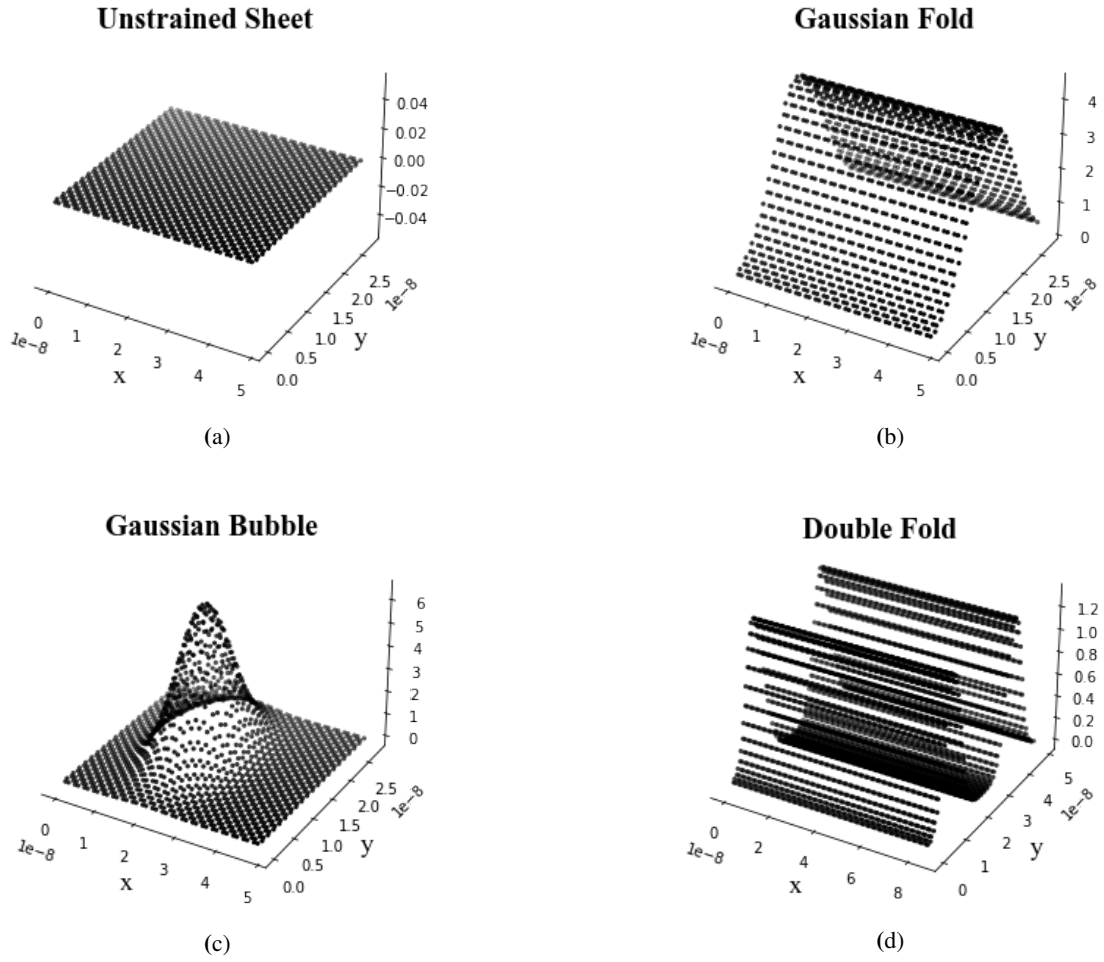
Unstrained Sheet

(a)

Gaussian Fold

(b)

Gaussian Bubble

(c)

Double Fold

(d)

Figure 1.9 (a) The un-strained 15 x 15 sheet presented in figure1.6 (b) now in three-dimensional space. **(b)** The Gaussian fold strain profile applied to the sheet, where $A_0 = 5nm$. $\sigma_y = 7.5nm$ and $y_0 \approx 15nm$. **(c)** The Gaussian Bubble strain profile applied to the sheet, where $A_0 = 5nm$. $\sigma_y = \sigma_x = 7.5nm$, $y_0 \approx 15nm$ and $x_0 \approx 20nm$. **(d)** The double Gaussian fold structure composed of a linear combination of single folds. In this case, $A_0 = 1nm$. $\sigma_y = 3.5nm$ are the same for both, and $y_{0a} \approx 10nm$ and $y_{0b} \approx 35nm$. The dimension of the double fold sheet is (35 x 35)

The second assumption corresponds to the hopping integral matrix element $\gamma \approx -2.8eV$ remaining constant throughout the lattice system, due to the absence of any impurities or mechanical strain. Lastly, the structure is finite, therefore, the finite Hamiltonian (2.1) is utilised, concerning the 5 x 5 unit cell structure (100 atoms). As a consequence of this, there is an obvious spatial distribution of the energy eigen-modes. The energy states which are exploitable and typically of interest, are the lowest energy-eigen states and are found at the half filling of the band structure, in this case, the lowest energy eigen-modes will be distributed around the zig-zag edges.

ii. The Infinite and Semi-infinite Hamiltonian

The model outlined in section 2.2.2 Refers to the formulation of the NNTB Hamiltonian under the assumption of an infinite periodic potential implicit in the Bloch formulation. This methodology is applied here to extract the electronic band structure confined to the first Brillouin zone (**fig 1.8 (a)**). The band structure is also observed about the **K** (**K'**) point. Alternatively, **fig 1.8 (b)** employs the semi-infinite model. For ease of computation **fig 1.8 (b)**, is achieved for $n_y \rightarrow 25$ using the Hamiltonian formulation outlined in (2.1). The explicit Hamiltonian implemented for the infinite potential takes the matrix form:

$$H(k) = \begin{bmatrix} 0 - \varepsilon(k) & \gamma(e^{ik\cdot\delta_1} + e^{ik\cdot\delta_2} + e^{ik\cdot\delta_3}) \\ \gamma(e^{-ik\cdot\delta_1} + e^{-ik\cdot\delta_2} + e^{-ik\cdot\delta_3}) & 0 - \varepsilon(k) \end{bmatrix}$$

(2.2)

Where δ_1, δ_2 and δ_3 refer to (1.1). In context of **fig 1.8 (a)** The band structure is computed along the k_x and k_y direction. The computation for k_x was confined within the bounds $[-2b_{1x}, 2b_{1x}]$. Similarly, the computation for k_y was confined to $[-2b_{1y}, 2b_{1y}]$, where b_1 is given in (1.4). The convergence of the conduction and valance bands can be seen clearly at the Dirac point in **fig 1.8(b)**. In both cases, the hopping integral $\gamma \approx 2.8eV$ was considered along with $\varepsilon = 0$.

3.2   Strain Geometries On Monolayer Graphene

Three out-of-plane strain geometries are applied and the emergent properties are studied and contrasted. All strain geometries considered are out of plane such that $\{(x,y,z) \in \mathbb{R}^3 | z = f(x,y)$ where $f(x,y) \equiv h(x,y)$ as mentioned previously and $f : \mathbb{R}^2 \rightarrow \mathbb{R}^3$. All functions are considered smooth and differentiable and chosen such that their derivatives will induce effective pseudo-gauge and pseudo-magnetic fields. The linear terms of the strain tensor, which correspond to the in-plane displacements are sufficiently omitted in this context [50]. Although these linear terms can infact produce an effective gauge field, they typically only give rise to the linear migration of
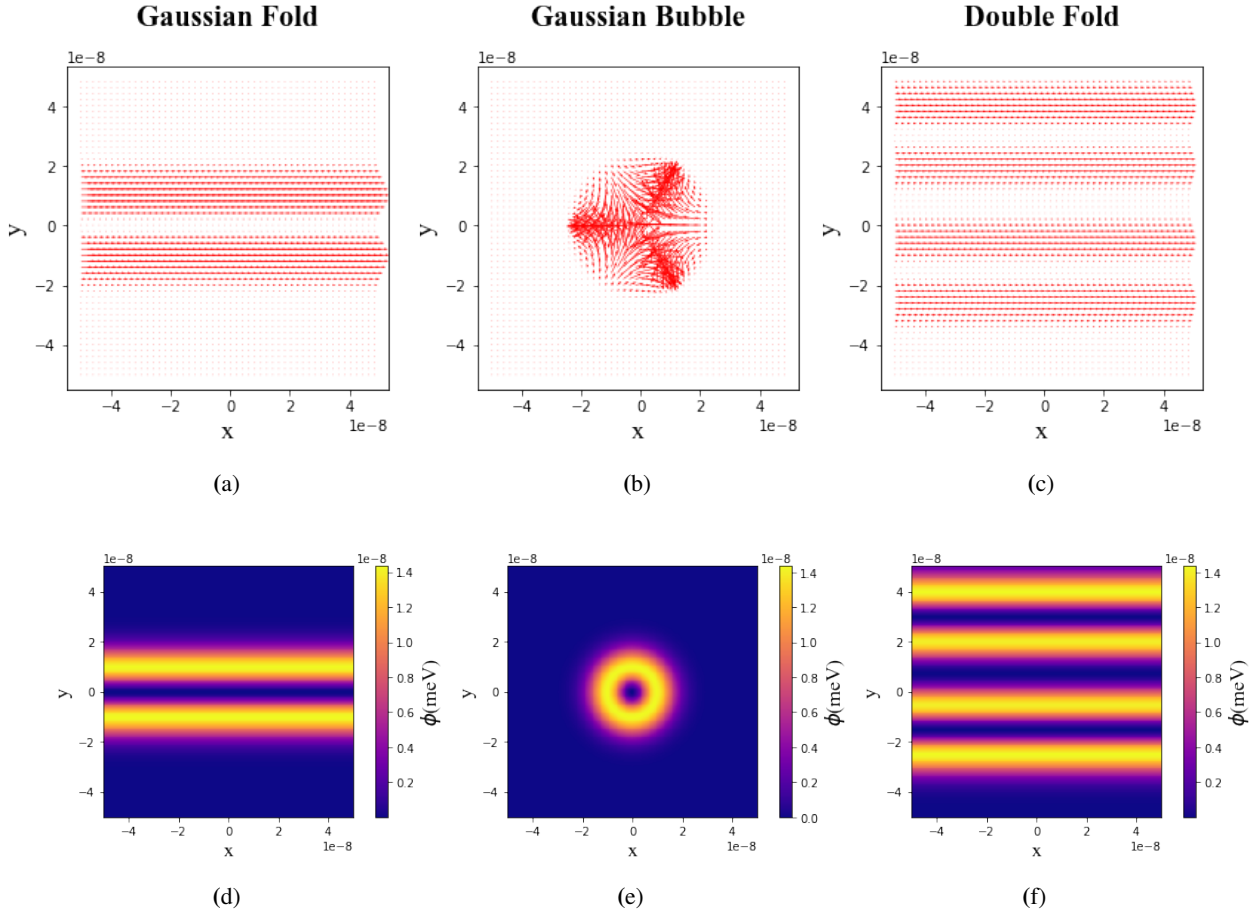
Gaussian Fold   **Gaussian Bubble**   **Double Fold**

(a)   (b)   (c)

(d)   (e)   (f)

Figure 2. The determination of the pseudo-gauge fields for each strain geometry outlined in fig. 1.9 was obtained via (1.54) using $\beta = 3.37$, $a_0 = 1.42$ Åand $e = 1.60210^{-19}$ C. **(a)-(c)** corresponds to the **K'** sub-lattice. point The scalar field constant $g_s \approx 3eV$ according to literature [50-51]. **(a)** Refers to the pseudo gauge field induced by the single Gaussian fold strain profile. **(b)** The pseudo gauge field induced by the Gaussian bubble strain profile. **(c)** The pseudo gauge field induced by the double Gaussian fold strain profile. **(d)**

the Dirac cones from their crystallographic symmetry (**K** and **K'**) points in the Brillouin zone. The uniformity in the linear strain is equivalent to a constant effective gauge field which does not vary spatially[10][18]. The first strain geometry studied corresponds to an extended Gaussian fold distribution. This geometry was imposed onto the x-y plane of a 25 x 25 sheet of monolayer graphene. The strain distribution was confined to a single dimension and remained invariant along the other. The second strain geometry consisted of a centrosymmetric Gaussian bubble, which takes the form of the bivariate Gaussian distribution. This strain was also applied to the x-y plane of a 25 x 25 sheet of monolayer graphene and the peak of the distribution was localised at approximately the centre of the sheet. The final geometry consisted of a periodic Gaussian structure. In particular, this structure consisted of two-fold distribution formed by the linear combination of the Gaussian folds functions outlined previously. The centres of each fold were situated at different points along e_y such that there formed a significant gap between each curves. The exception in this case, was simply that the double fold distribution was applied to a larger 35 x 35 sheet of monolayer graphene to accommodate for the occupancy of two curves. The contour of the plots for each of the strain geometries can be seen in figure 2.8 in Appendix ix.

3.2.1   Gaussian Fold

The Gaussian fold strain geometry was modeled by the following function:

$$h(r) = A_0 e^{-R_y/2\sigma_y^2} \qquad (2.2)$$

Where $R_y = (y_i - y_0)^2$, such that y_0 corresponds to the centre of the peak. *sigma$_y$*, corresponds to the width or broadening of the curve about the y-axis and A_0 is the straining amplitude above the flat plane. The strain was confined to a single, direction, varying over the e_y direction, leaving lattice points traversing the e_x direction invariant. Figure 1.9 (b) shows the Gaussian Fold strain distribution for the 25 x 25 sheet of graphene. The emergent pseudo-gauge and pseudo-magnetic fields along with the scalar potential from this particular stain profile are discussed qualitatively in section 3.3. **Figure 2 (a),(d)** and **Figure 2.1 (a)(c)** demonstrate these properties.

3.2.2   Gaussian Bubble

The Gaussian Bubble strain was modeled by the function:

$$h(r) = A_0 e^{(-R_y/2\sigma_y^2)-(R_x/2\sigma_x^2)} \qquad (2.2)$$

Once again $R_y = (y_i - y_0)^2$ and similarly $R_x = (x_i - x_0)^2$. Typically the width of the bubble $\sigma_y = \sigma_x$ for a centrosymmetric distribution. The Bubble is centred about the points (x_0, y_0), which is approximately at the centre of the sheet. Figure 1.9 (c) shows the Gaussian Bubble strain distribution for the 25 x 25
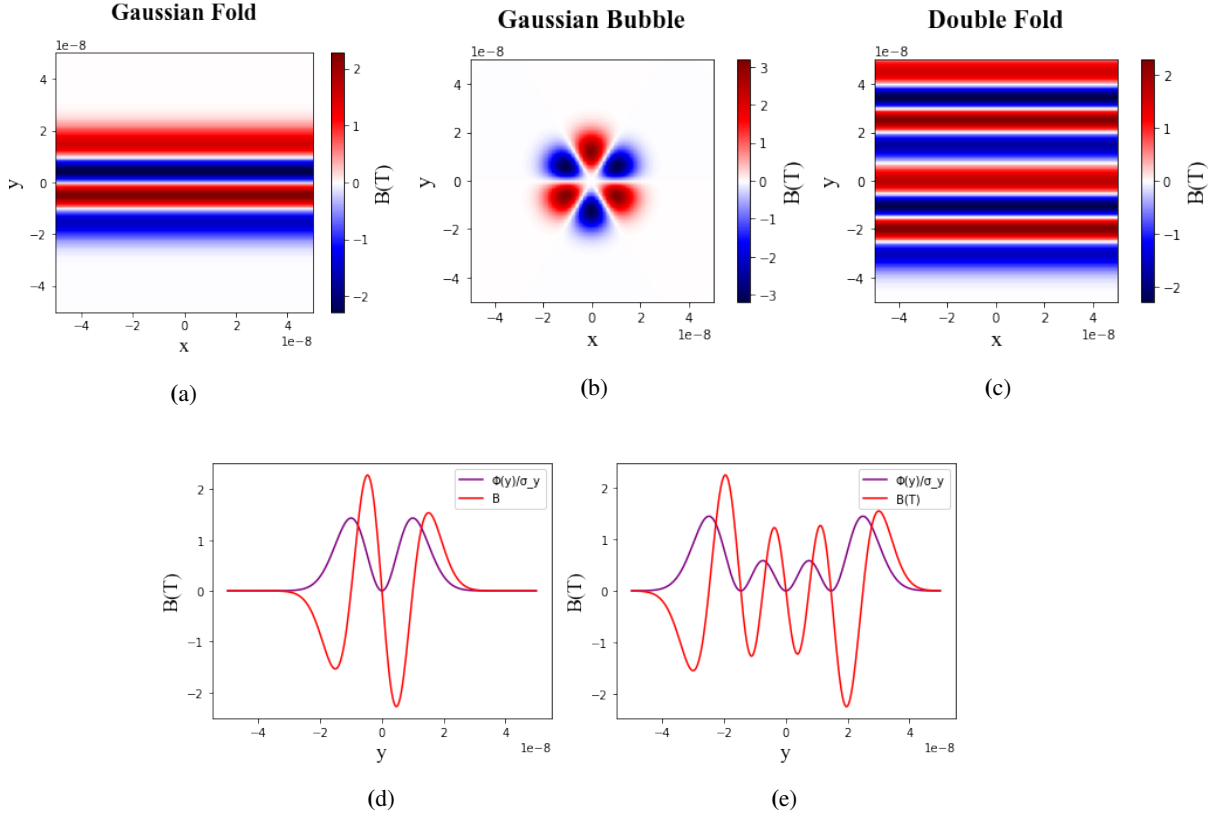
Figure 2.1 The determination of the pseudo-magnetic fields for each strain geometry outlined in fig. 1.9 was obtained via (1.58) using $\beta = 3.37$, $a_0 = 1.42$ Åand $e = 1.60210^{-19}$ C. **(a)-(c)** corresponds to the **K'** sub-lattice **(a)** Refers to the pseudo-magnetic field induced by the single Gaussian fold strain profile. **(b)** The pseudo-magnetic field induced by the Gaussian bubble strain profile. **(c)** The pseudo-magnetic field induced by the double Gaussian fold strain profile. **(d)** Cross section of the scalar potential and the PMF for the single Gaussian fold.**(e)**Cross section of the scalar potential and the PMF for the double Gaussian fold. The PMF scale is measured in Tesla, the scalar potential is scaled down by a factor of σ_y

sheet of graphene. The emergent properties from this particular stain profile are also discussed in section 3.3.

3.2.3   Periodic Gaussian Ripple

The Periodic Gaussian ripple strain was modeled by the function:

$$h(r) = A_0 e^{-R_{y1}/2\sigma_y^2} + A_0 e^{-R_{y2}/2\sigma_y^2}$$
$$\equiv A_0(e^{-R_{y1}/2\sigma_y^2} + e^{-R_{y2}/2\sigma_y^2}) \qquad (2.3)$$

Two symmetrical folds are produced; by factoring out A_0 one can produce two folds with identical amplitudes. σ_y is identical for both folds. The $R_{y1} = (y_i - y_{01})^2$ and $R_{y2} = (y_i - y_{02})^2$ terms differ such that the midpoints of each distribution are situated far enough apart from each-other in order to produce a sizable vale between the folds. Figure 1.9 (d) shows the Gaussian Fold strain distribution for the 35 x 35 sheet of graphene.

3.3   The Continuum Dirac Model

It has already been established in section 2.4 that the implementation of smooth, out-of-plane strain provokes small perturbations to components of the effective Dirac Hamiltonian in the form of pseudo-gauge **A** and pseudo-scalar fields **phi**, i.e:

$$H(\mathbf{q})_{K,K'} = v_F \boldsymbol{\sigma} \cdot (\mathbf{q} \pm e\mathbf{A}) + \phi(r)\sigma_0 \qquad (2.3)$$

Therefore through the relation (1.58) emerges the Pseudo-magnetic fields. The inhomogeneous characteristics of the strain profiles produce inhomogeneous pseudo-magnetic fields, which pertain characteristics identical to that of real magnetic

fields, (With the exception of the parity interchanges in the in-equivalent valleys) therefore, such effects attributed to the dynamics of electrons in real magnetic fields can be seen in these contexts. In this Dirac formalism, the low energy states will incur localisation due to the presence strain induced gauge fields [57-58], thus the local density of states will change correspondingly. The confinement is typically associated with the strong emergent pseudo-magnetic fields (which have shown to occur up to an excess of 300T experimentally [59]). **Figures 2**, **Figures 2.1**, **Figures 2.2** and **Figures 2.3** display the emergent fields from the strain geometries. **Figures 2** and **2.1** correspond to the emergent fields at the **K'** sub-lattice point, whilst **Figures 2.2** and **2.3** correspond to the **K** point, with disparities due to the property $\mathbf{A} \rightarrow -\mathbf{A}$ in the separate valley regions as discussed earlier. Moreover, it has been shown extensively that the implications of smooth strain (which does not merge in-equivalent valleys) produces a sub-lattice symmetry breaking between both valleys regarding the electronic spectrum [57] (see **Figure 2.1** and **Figure 2.2** In which the PMF and PGF for both the **K** and **K'** points were determined. The breaking of the sub-lattice symmetry in the continuum description has been shown to produce pseudo-spin polarization induced by the coupling of the pseudo-magnetic field of the confined of electrons in each of the positive and negative valley regions [60]. However, due to the quasi-relativistic fermions, Klein tunneling and potential scattering renders electron confinement in graphene to be more involved. The pseudo-magnetic fields emerge orthogonally to the lattice plane, therefore at the boundaries
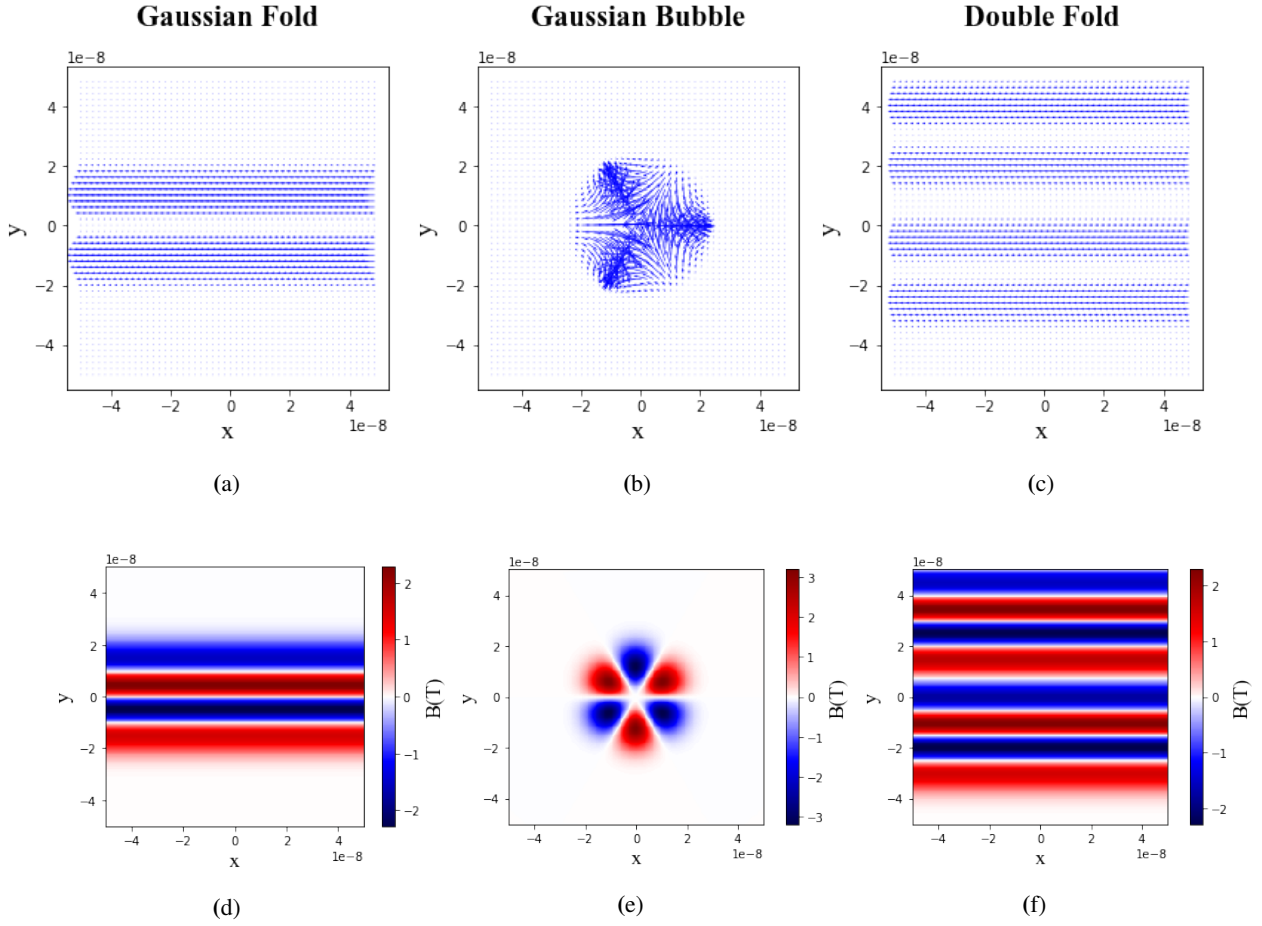
Gaussian Fold

(a)

Gaussian Bubble

(b)

Double Fold

(c)

(d)

(e)

(f)

Figure 2.2 The determination of the pseudo-gauge fields and the pseudo magnetic fields for each strain geometry outlined in fig. 1.9 was obtained via (1.54) using $\beta = 3.37$, $a_0 = 1.42$ Å and $e = 1.602 10^{-19}$ C. **(a)-(c)** correspond to the **K** sub-lattice. **(a)** Refers to the pseudo gauge field induced by the single Gaussian fold strain profile. **(b)** The pseudo gauge field induced by the Gaussian bubble strain profile. **(c)** The pseudo gauge field induced by the double Gaussian fold strain profile. **(d)** Regards the PMF due to the Gaussian fold distribution. **(e)** corresponds to the PMF due to the Gaussian Bubble. **(f)** PMF due to the double Gaussian fold.

between the positive and negative field regions (blue - red regions in **figure 2.1, 2.2**) the charge carriers traverse in so called "snake-state" trajectory as a consequence of the change in direction of the Lorentz force. The local density of states is maximised at the extremities of each PMF i.e the majority of states reside at the crests and troughs of the Gaussian fold And the Double fold geometry whilst in the Gaussian Bubble geometry, the charge carriers reside in each 'petal' of the sixfold symmetric region upon the surface of the bubble [61]. In the context of pristine graphene, at half-filling of the band, the Fermi level (zeroth energy state) subsists at the Dirac point and the density of states for the linear 2D dispersion regime disappears [62]. In pragmatic graphene technologies the Fermi level can be adjusted using the gate voltages, in strain-tronic devices the location of this point can be altered significantly. This is imperative to the realization of bound modes within graphene wave-guides, as zero-energy modes cannot escape into the bulk states as there are no states to tunnel into. Expressions (2.4) - (2.6) correspond to the emergent fields associated with the K' sub-lattice region, for the K expression, its simply calculated by the same procedure under the substitution $-\mathbf{A} \to \mathbf{A}$. **Figure 2(a)** demonstrates the emergent pseudo-gauge field (PGF) corresponding to the single Gaussian fold strain geometry characterised by (2.2).**Figure 2(d)** Beneath displays the scalar field potential consequent from the redistribution of charges. This quantity is defined by $\phi(r) = g_s(\varepsilon_{xx} + \varepsilon_{yy})$, more explicitly, both

the pseudo gauge field $\mathbf{A}$ and scalar potential ϕ in this context are defined by:

$$GaussianFold = \begin{cases} \mathbf{A} = -\frac{\beta}{2ea_0}\Lambda_y e^{-R_y/\sigma_y^2} \\ \phi = g_s\Lambda_y e^{-R_y/\sigma_y^2} \end{cases} \tag{2.4}$$

The corresponding pseudo-magnetic field for this strain distribution can be found in **Figure 2.1 (a),(d)**. Alternatively, the associated PGF and PMF for the K sub-lattice point can be seen in **Figure 2.2 (a), (d)**. The difference between both is clear, due to the change of sign in each valley, the crests and troughs effectively switch. i.e blue (negative) $\to$ red (positive).

Similarly, **Figure 2(b)** and **Figure 2(e)** demonstrates the PGF (K') and scalar potential for the Gaussian Bubble strain respectively. Explicitly, these take the form:

$$GaussianBubble = \begin{cases} \mathbf{A} = -\frac{\beta}{2ea_0}e^{(-R_y/\sigma_y^2)-(R_x/\sigma_x)}\begin{pmatrix} \Lambda_x - \Lambda_y \\ -2\Lambda_x\Lambda_y \end{pmatrix} \\ \phi = g_s e^{(-R_y/\sigma_y^2)-(R_x/\sigma_x)}(\Lambda_x + \Lambda_y) \end{cases} \tag{2.5}$$

Once again The K' PMF distribution is shown in **Figure 2.1 (b)** whilst the K sub-lattice point PGF and PMF distributions can be seen in **Figure 2.2 (b) (c)**.

PMF Gaussian fold   PMF Gaussian Bubble   PMF Double Fold
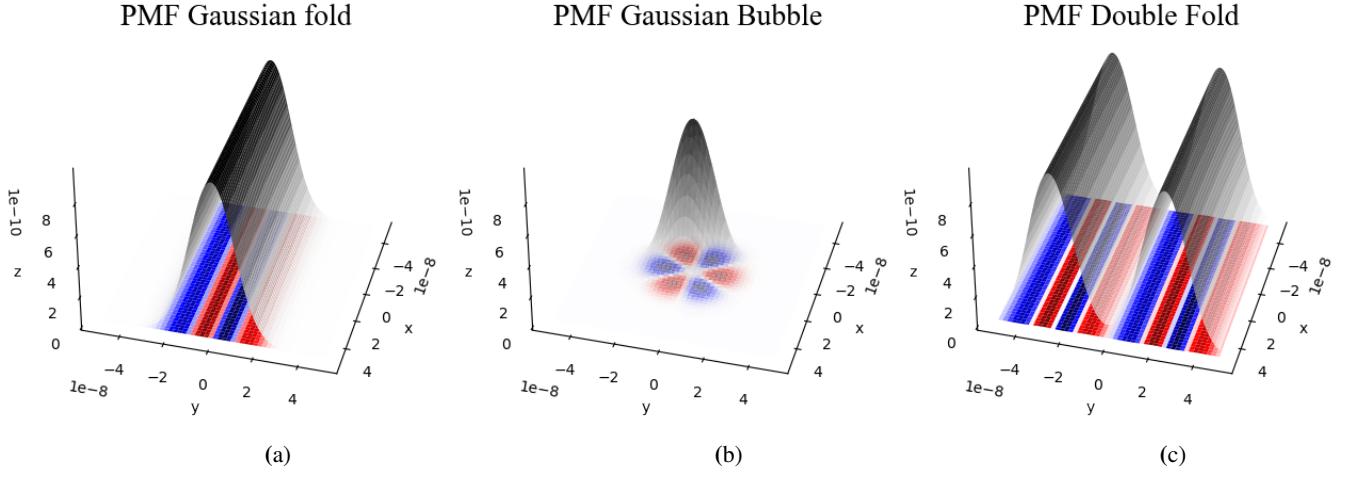
(a)   (b)   (c)

Figure 2.3 The projection of the PMFs onto the real-space plane of the strained lattice geometry. Representations correspond to the K sub-lattice point. Regions where the magnetic fields change i.e red → blue define the regions where the snake-states reside. **(a)** snake states exist on the peak of the fold **(b)** sixfold 'petal' symmetry consisting a two sets of positive and negative PMF regions. **(c)** The double fold region has the ability to produce snake states at each peak and also at the trough, where both folds create a vale.

Lastly, **Figure 2(c)** and **Figure 2(f)** demonstrate the PGF (K') and scalar potential for the double fold Gaussian strain geometry. These have the explicit form:

$$DoubleFold = \begin{cases} \mathbf{A} = -\frac{\beta}{2ea_0}\left(\Lambda_y e^{-R_y/\sigma_y^2} + \Lambda_{y1} e^{-R_{y1}/\sigma_y^2}\right) \\ \phi = g_s\left(\Lambda_y e^{-R_y/\sigma_y^2} + \Lambda_{y1} e^{-R_{y1}/\sigma_y^2}\right) \end{cases}$$

(2.6)

present in each case are the Λ_x and Λ_y terms, which are simply just constants of derivatives such that: $\Lambda_y = A_0^2(y_i - y_0)^2/\sigma_y^4$, $\Lambda_x = A_0^2(x_i - x_0)^2/\sigma_x^4$. The Λ_{y1} term is the constant of the derivative corresponding to the second fold at position y_{01}. The emergent PMF for each case is determined by the relation outlined previously ($B = \nabla \times \mathbf{A}$).

Figure 2.3 qualitatively demonstrates the projection of the associated PMFs onto the real-space plane of the individual strain profiles. An important distinction is of course is that the field directions are described by the colour i.e. red = positive, upwards and blue = negative, downwards. The magnitude of the fields are outlined correspondingly in **Figure 2.2 (d) - (f)** for a strain amplitude of 1nm. For the case of the single Gaussian fold geometry, the interchanging PMF occurs at the crest of the profile, at the central zeroth-magnetic field region, therefore, one would expect to see snake-states existing within that region. Similarly, for the double fold geometry, snake states occur on both fold crests with the addition of another region located in the vale between both fold profiles.

In particular, observing the region confined between the two folds where the positive and negative PMF region emerges in **Figure 2.3 (c)** and **Figure 2.4** below, considering that snake states are parameterised by the quasi-classical cyclotron diameter: $2R_c = 2\hbar k/e\mathbf{B} = 2h\sqrt{n\pi}/eB$ [38], implies that for certain strain regimes, the states confined to the vale region will perhaps exist momentarily, but then proceed to drift either left or right. The direction of the drift depends on a multitude of factors. Firstly, the relative valley origin of the charge plays a role. As seen in this context to **Figure 2.4**, there exists snake trajectories up and down the region as a consequence of K and K' valley regions, which have respective clockwise and anticlockwise cyclotron orbits. **Figure 2.4** corresponds to the

K sub-lattice valley region. Secondly, the relative size of $2R_c$ with respect to the span of the blue-red (positive-negative) field region or the magnetic length ($l_B = sqrt\hbar/eB$, has an effect of the snake states through the cyclotron relation; thus implying a dependency on the strength of the pseudo-magnetic field, which of course is dependent on the magnitude of the strain. Therefore, to prevent elongated snake states from drifting, snake-state trajectories must follow the condition $2R_c < L_B$. However, in the cases of the single Gaussian fold and double Gaussian fold geometries, we have significantly better confinement of the snake trajectories in the latter, primarily due to the physical barriers (lattice folds) provided by the double fold geometry. This infers that the electrons confined between the folds (in the vale) will diverge significantly less than snake-states present on the crests of the folds, in the context of the above conditions.
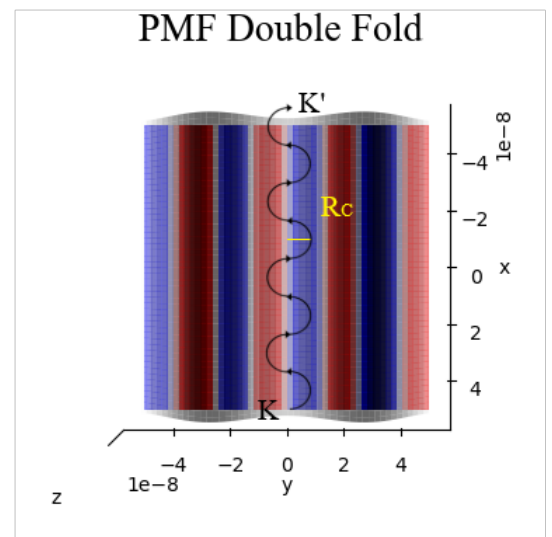

PMF Double Fold

Figure 2.4 Snake states emergent between fold regions. Valley polarized currents denoted by **K** and **K'**

As mentioned previously, confinement of electrons have shown to occur along the extremities of the fold geometries as a consequence of the redistribution of the LDOS, therefore it is
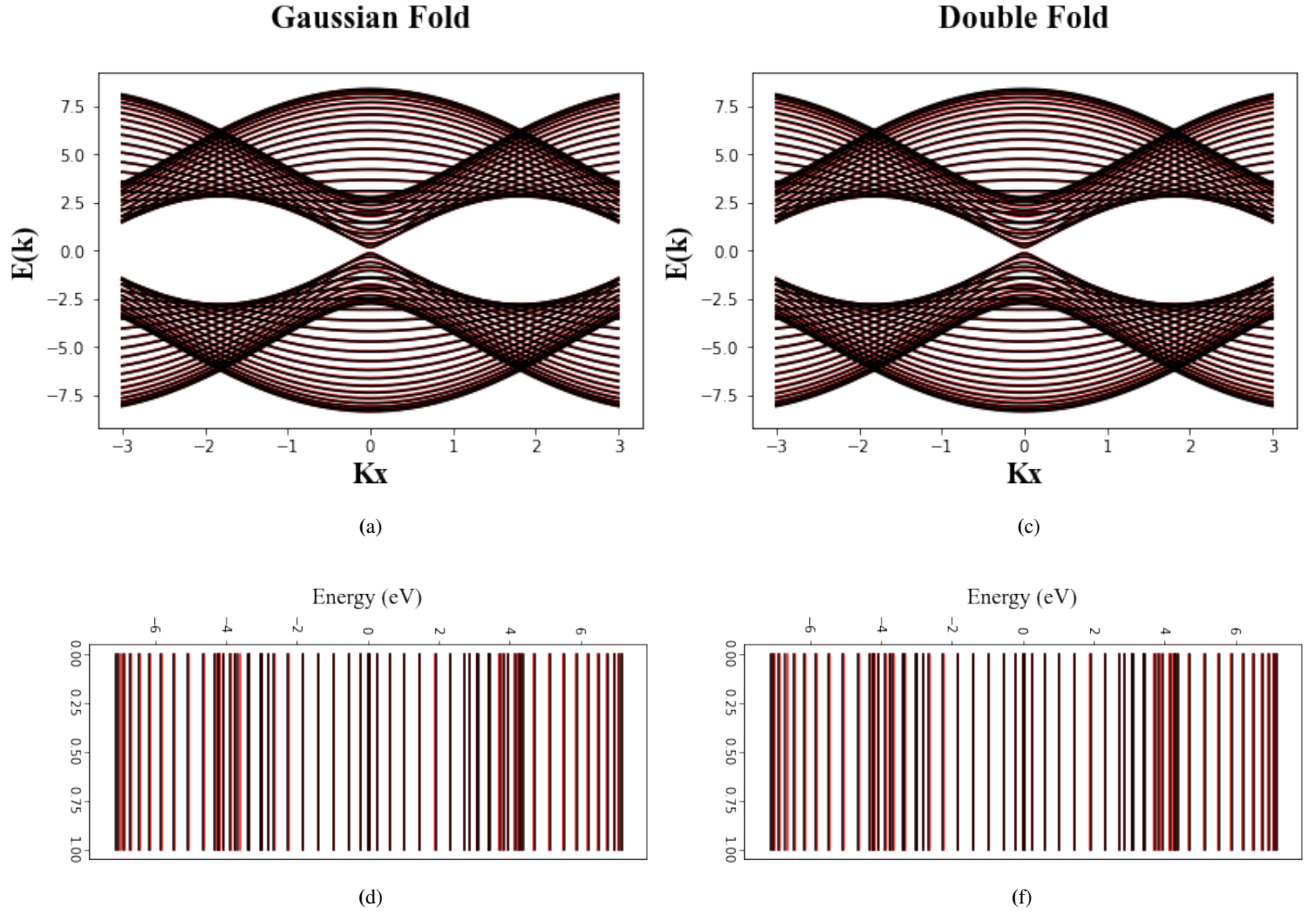
Gaussian Fold   ## Double Fold

(a)   (c)

(d)   (f)

Figure 2.5 The band structures calculated for each respective strain geometry. The red overlay corresponds to the new modulated bands formed from straining, whilst the black corresponds to the unstrained system. **(a)-(b)** Are the band structures for each case of the fold strains **(d)-(e)** Displays the real eigen-value spectra for each case of strain. The model parameters were confined to $n_y = 15$ with a strain amplitude of 3.5 Å and a broadening of $\sigma_y = 2$

proposed that strained graphene systems can infact act as a 1D nanowire structures with quantized conductance. Heuristically, this can be shown: Consider the simplest case, of idealised graphene; (such that structural inhomogenieties are negated along with scattering processes) strained by a Gaussian fold such as **Figure 2.3 (a)**. Suppose two electrodes are placed at either end of the "effective" quantum wire, or folded region, one being a source μ_s and the other being a drain μ_d for the purpose of creating a bias voltage V_b such that $\Delta\mu = \mu_s - \mu_d = eV_b$. The current induced by V_b is generally given by $I = eN/\tau$, where N is the number of charge carriers, e is elementary charge and τ is the time it takes to traverse the quantum wire of length L. For small $\Delta\mu$, such that one is close to the Fermi level and within the linear dispersion regime, the Fermi velocity can be defined explicitly as $v_F = 1/\hbar \cdot dE/dk$, therefore the time τ can be expressed as $\tau = L/v_F$. Now, to finally obtain the expression for I, the quantity of electrons N is determined by:

$$N = 2_s \cdot 2_v \int_{k_{\mu_d}}^{k_{\mu_s}} \frac{dk}{2\pi/L} \tag{2.7}$$

Where $2_s, 2_v$ correspond to the spin and valley degeneracy of the electrons and $\Delta k = 2\pi/L$ corresponds to the space between states at each k within the length of the wire. Now, substituting

into the expression for I :

$$I = 4 \int_{k_{\mu_d}}^{k_{\mu_s}} \frac{dk}{2\pi/L} \frac{1}{\hbar L} \frac{dE}{dk}$$

$$I = \frac{2e}{h} \Delta\mu$$

$$\Rightarrow I = \frac{4e^2}{h} V_d s \tag{2.8}$$

Where $\sigma \approx 4e^2/h = G_0$, which is referred to as the quantum conductance and $V_d s = \Delta\mu/e$. Its obvious that G_0 is a constant irrespective of the cross-sectional area, specific resistance and length of the material used. However, the remarkable property with these additional conductance channels formed by strain, they also have the property of being valley polarized [62]. Alternatively, more conventional methods utilise the eigen-states (1.46) of the Dirac Hamiltonian to achieve the conductance in pristine via analysis of scattering processes [50]. Moreover, methods outlined in [64] achieves the conductance of graphene through the Landauer formulation. The same physical parameters are established such that a finite nano-ribbon is considered, with corresponding lengths $'L'$ and widths $'W'$, which is connected to electrodes lengthwise, providing a similar bias voltage. Conclusively, the paper suggests that the
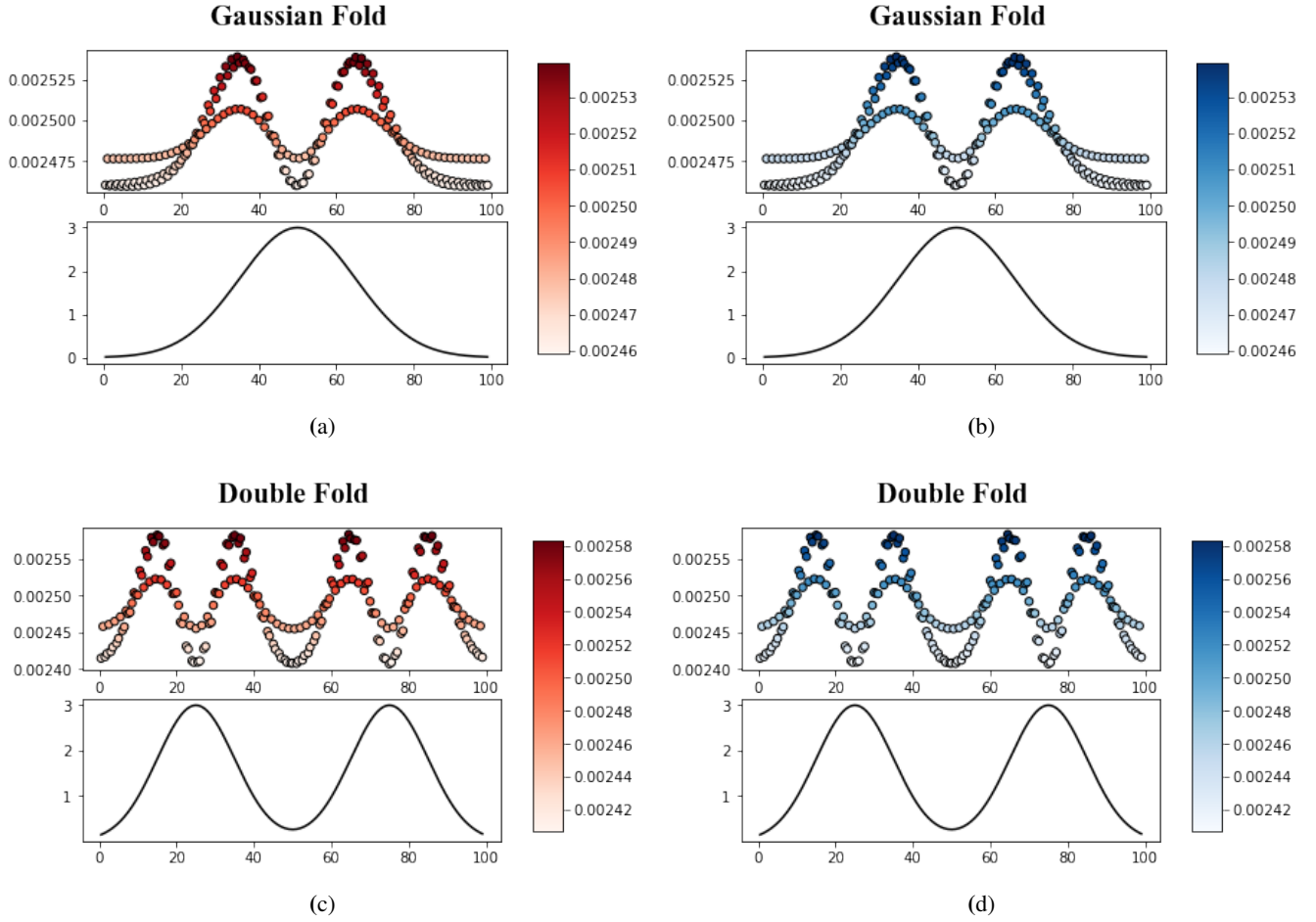
(a)

(b)

(c)

(d)

Figure 2.6 The probability densities corresponding to the single and the double Gaussian fold distribution via the semi-infinite model for specific energies 0.15eV in opposing velocity groups corresponding to the **K** and **K'** valleys. The strain parameters are as such: $n_y = 100$, $\sigma_y = 15$ A = 3. **(a)-(b)** correspond to the probability densities of the **K** and **K'** valleys respectively. Likewise **(c)-(d)** Are the subsequent probability densities of states in the double fold geometry.

conductance of a graphene sheet has a dependency on its dimensions, more specifically the ratio between its length and width i.e. $\Rightarrow \sigma = (L/W)G$, Where G is the Landauer formula, unlike the heuristic approach outlined in (2.8). However, for regimes in which $W/L \gg 1$, σ infact reduces to (2.8). In either case, the formulation for σ is only accurate in systems which have a narrow relation W/L. Moreover, results outlined in [63], utilising the Landauer method previously discussed, in the explicit case of a Gaussian fold profile demonstrated that with increasing strain the conductance channels opens up from the previously described two sets of spin and valley degeneracy current channels to six as a consequence of sub-lattice polarized states localising around the strained area, induced by the breaking of the sub-lattice symmetry. These wave-guides can be polarised as such, in accordance to their valley origin, providing a novel way of transmitting information.

3.4   The NNTB Model for Strained Systems

The analysis of the modulated electronic properties induced from each case of the fold strain geometry is achieved through the NNTB method outlined in sections **2.2** and **3.1 (ii)**. The Gaussian bubble case is omitted here as the semi-infinite model is confined explicitly to a single dimension e_y. The explicit implementation for the computation for the band structures and energy spectra is outlined in Appendix iv. The NNTB approach

employs the semi-finite method previously outlined, in order to compute the eigen-spectra and electronic transport properties of graphene for each instance of applicable strain. For ease of computation and to illustrate the effects of strain, the dimensions are confined to $n_y = 15$ whereas of course $n_x = 1$. The strain parameters for each case were modified in comparison to **Figure 1.9** to accommodate the dimensions of the model, with $\sigma_y = 2$ and a slightly larger strain amplitude of A = 3.5Å. **Figure 2.4** illustrates the effects of strain on the eigen-spectra of pristine graphene in juxtaposition with the strained system. The red overlay corresponds to the modulated band structure and energy levels as a consequence of strain, whilst the black corresponds to pristine graphene. Moreover, to provide a clearer elucidation of the alteration of the band structure and energy levels, **Figure 2.9** in the Appendix viii demonstrates the same system, now with reduced dimensions, such that $n_y = 5$, where one can see the shift in the band-structure and energy-levels more clearly. As expected the K and K' point slowly drift towards each-other in increasingly larger regimes of strain [11][18][54]. Moreover, as alluded to earlier, strain geometries induce pseudo-fields which play a role in the redistribution of the LDOS, with the majority of states now populating the strained region. However, more subtly, the redistribution of states are now separated by their valley indices, with states originating from the **K** having larger probability densities on the centre of the strain peaks,

whilst **K'** points having larger probability densities on the sides of the strain geometry. **Figure 2.6** Displays the probability densities ψ^2 regarding the wave functions of states across the entire lattice structure for **K** and **K'** respectively. More specifically, the wave-functions described correspond to specific crystallographic momenta k_1 and k_1 which have approximate defined energy 0.15eV and are located in the vicinity of the Dirac point. Both probability density distributions outlined have contributions from the A and B neighbouring sub-lattice sites. The focus here is to demonstrate the redistribution of states to the regions of strain for the purpose of confinement and wave-guiding.

4 Conclusion and Evaluation

The analysis of strained graphene systems was conducted under two coupled, yet distinct frameworks. Firstly, the Dirac continuum formalism provided for the existence of of strain-induced pseudo-gauge and pseudo-magnetic fields present within graphene systems that were explicitly subject to inhomogeneous out-of-plane strain. Secondly, the modulation of the hopping integral element pertinent to the NNTB formalism results as a consequence of this inhomogeneous lattice strain, where its shown that the modulation of the hopping integral element is deduced by the continuum elasticity model. This model provides for the coupling of the two frameworks in contexts of strain, where it has been shown that the presence of strain accounts for small perturbations in the Dirac-like Hamiltonian in the form of a pseudo-gauge field. This emergent pseudo-gauge field now has a spatial dependency, which further implies the existence of pseudo-magnetic field as a consequence of its non-vanishing curl. In particular, Gaussian profiles such as extended folds, bubbles and double folds have been implemented and their effects have been discussed. Certain strain profiles provide for the ability to act as 'nano-wires', in which some contexts, the boundary region where the pseudo-magnetic field changes direction implies for the manifestation of "snake-state" trajectories, characterised by semi-classical cyclotron orbits. The imposition of strain has been shown to alter the intrinsic electronic properties of graphene, where calculations utilising the NNTB formalism demonstrate the shift in graphenes electronic and structure and energy levels. In particular, the semi-infinite model was employed to analyse two Gaussian strain geometries, namely the single an double Gaussian fold. In each case, the determination of the band structures and energy-levels were shown. The probability density distribution furthers the claim that the PMFs tend to localize charges in the regions of the folds. The aspect regarding scattering and tunnelling processes was unfortunately not achieved, however, I outline briefly the premise of those concepts in regards to waveguides.

4.1 What I would have liked to achieve.

4.1.1 Confinement, Scattering processes, Transmission and Reflection

In order to achieve a better quantitative understanding of confinement and wave-guiding electrons in systems such as strained graphene, one must analyse the processes the multitude of effects associated with electron scattering and Klein tunnelling. More specifically, I would have liked to analyse the scattering processes between the emergent pseudo-gauge field profile (**figure. 2, 2.1**) for the single Gaussian fold geometry, where the emergent gauge-field acts as an effective double potential barrier problem, synonymous to the prominent rectangular potential barrier problem demonstrated in quan-

tum mechanics. From this I could determine the transmission and reflection coefficients associated with the confined states within the fold region. In-fact, the necessary requirements to describe the confined states within this fold region is encapsulated within the problem for the single-barrier potential, therefore the problem becomes less involved. The problem can be solved by firstly configuring the boundary conditions by approximating the gauge-field geometry as a single-rectangular potential barrier such that the gauge field no longer has a spatial dependency, (although this may suggest that $\mathbf{B_{ps}}$ is non existent due to the vanishing curl of **A**, its merely a simplification of the problem), therefore **A** = constant, $y \in [y_1, y_2]$. The analysis regards the wave-functions corresponding to the regions in the low-energy dispersion regime outlined in (1.44, 1.45, 1.55), therefore, for the electrons which reside on either side of the barrier i.e $y < y_1$ and $y_2 < y$ the particle has energy $E = \pm_F ||$ and for $y \in [y_1, y_2]$ the particle has energy $E =_F || \pm e\mathbf{A}$. The figure below demonstrates the simple single-potential barrier:

Single Barrier Approximation

$y < y_1$ $y \in [y_1, y_2]$ $y_2 < y$
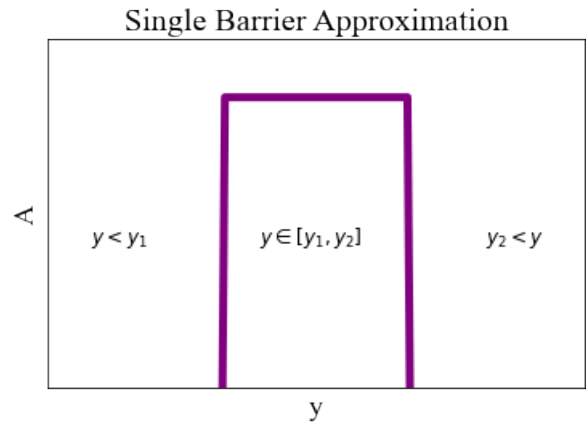
Figure 2.7 Single barrier potential problem induced by the presence of an effective gauge field.

The corresponding wave-functions for the electrons regarding the boundary conditions take the form:

$$\Psi = \begin{cases} C_2 \begin{pmatrix} 1 \\ k_x + ik_y/k \end{pmatrix} e^{ik_x x} e^{ik_y y} + C_1 \begin{pmatrix} 1 \\ k_x - ik_y/k \end{pmatrix} e^{ik_x x} e^{-ik_y y} \\ \\ C_3 \begin{pmatrix} 1 \\ e^{i\phi} + ik_y/k \end{pmatrix} e^{ik_x x} e^{iq_y y} + C_4 \begin{pmatrix} 1 \\ e^{-i\phi} \end{pmatrix} e^{ik_x x} e^{-iq_y y} \end{cases} \tag{2.9}$$

for $y < y_1$ and $y_2 < y$ and $y \in [y_1, y_2]$ respectively. The $C_i, i = 1, 2, 3, 4$ terms are normalisation constants of the wave-functions. $k_x = \mathbf{k}\cos\theta$ and $k_Y = \mathbf{k}\sin\theta$, correspond to the momenta outside of the barrier region, obtained from the linear dispersion regime outlined above. Each have a dependency in the angle of incidence on the barrier region with respect to 'y'. The modulated momentum of the electron within the barrier as a consequence of the emerged pseudo-gauge field is determined by (for the **K'** valley region):

$$q_y - \frac{1}{F}\sqrt{E^2 - (_F k_x - v_F A_x)^2} \tag{2.10}$$

From this deduction, the transmission and reflection coefficients can be calculated from these wave-functions. From this point, the energy vs the angle of incidence θ of the confined states can be determined where, it has been shown that higher energies are more probable of transmission. A very unique

property emerges, that the transmission probabilities effectively "switch" for the **K** and **K'** points, meaning that for no transmission corresponding to lower angles of electrons from one valley region, will imply highly probable transmission for the other and vice versa. The reintroduction of the second barrier potential, that exist due to the Gaussian fold, is an imperative feature for the channeling electrons. A linear combination of the wave-functions seen in (2.9) can be constructed to describe the states existing between the double barrier regions. As a consequence of these effectively two square barriers, the wave-function within this region will behave like a standing wave, bound in the direction of the strain y, due to the exponential decay of the wave-functions inside each barrier. These modes have the ability to propagate along the direction in which the fold is invariant, x, enabling for the transport of electrons. Unfortunately, due to constraints on time, I was not able to investigate this aspect of the project, despite it being an imperative aspect in the evaluation of the transport regimes in strained graphene systems.

4.1.2   Further Analysis Utilising NNTB Calculations

I feel as if the quantitative approach was undercut due to time constraints, and I would have wished to conduct much more numerical analysis in regards to the NNTB formulation in the context of strain.

Appendix

i. Code: Unit Cell

```python
import numpy as np
import matplotlib.pyplot as plt
from matplotlib import cm
import pandas as pd
import matplotlib.patches as mpatches
from mpl_toolkits.mplot3d import Axes3D
from scipy import constants
#--------------------------------Graphene Geometry------------------------------------#

a = 1.42*10E-10   #Lattice constant
acc = a/np.sqrt(3)

Unitcell_x = np.array([0, a/(2*np.sqrt(3)), a*np.sqrt(3)/2, 2*a/np.sqrt(3) ])
Unitcell_y = np.array([0.5*a, 0, 0, 0.5*a])
Unitcell_s = np.array([1,-1,1,-1])

a1 = np.array([np.sqrt(3)*a, 0])
a2 = np.array([0, a])
#------------------------------------------------------------------------------------#
csfont = {'fontname':'Times New Roman'}
fig, ax = plt.subplots()
ax.set_aspect('equal')
ax.set_title("4-sublattice Unit Cell", fontsize=20, **csfont)
plt.xlabel('Armchair Direction', fontsize=17.5, **csfont)
plt.ylabel('Zig Zag Direction', fontsize=17.5, **csfont)
ax.plot(Unitcell_x, Unitcell_y, 'o--',c='purple', markersize=20)
ax.plot(Unitcell_x[1], Unitcell_y[1], 'o--',c='black', markersize=20)
ax.plot(Unitcell_x[3], Unitcell_y[3], 'o--',c='black', markersize=20)
ax.arrow(0, 0, a1[0], a1[1],fc='black',ec='black', width=0.2*10E-10)
ax.arrow(0, 0, a2[0], a2[1],fc='black',ec='black', width=0.2*10E-10)
ax.spines['top'].set_visible(False)
ax.spines['right'].set_visible(False)
plt.show()
```

ii. Code: Graphene Sheet

```python
#Sheet dimensions
n_x = 15
n_y = 15
x = np.array([])
y = np.array([])
sublattice = np.array([])
for i in np.arange(n_x):
    for j in np.arange(n_y):
        x = np.concatenate( (x,  Unitcell_x + i * a1[0] + j* a2[0]) )
        y = np.concatenate( (y,  Unitcell_y + i * a1[1] + j *a2[1]))
        sublattice = np.concatenate ( (sublattice, Unitcell_s))
fig, ax = plt.subplots()
ax.set_aspect('equal')
ax.set_title("5 x 5 Monolayer Graphene", fontsize=20, **csfont, x= 0.55, y=1.1)
plt.xlabel('Armchair Direction', fontsize=17.5, **csfont)
plt.ylabel('Zig Zag Direction', fontsize=17.5, **csfont)
ax.plot(x[np.where(sublattice==1)], y[np.where(sublattice==1)], 'o',
markersize=4,c='purple')
ax.plot(x[np.where(sublattice==-1)], y[np.where(sublattice==-1)], 'o',
markersize=4,c='black')
```

iii. Code: Real-space Hamiltonian, Energy spectrum, DOS

```python
#----------------Real space Hamiltonian generator for the finite sheet.----------------#
t0 = -2.8
epsilon = 0.02

positions = np.array((x, y)).T
dist = distance_matrix(positions, positions)
hops=np.isclose(dist, acc )
H = np.where(hops==True, t0, 0.0)
onsite_E = epsilon* np.ones((n))
H = H + np.diag(onsiteE)

#-------------------------------------Energy Spectrum-------------------------------------#
#Solving for the eigenvalues, eigenvectors.
eigenvalues, eigenvectors = np.linalg.eig(H)
elements = eigenvalues.argsort()
eigenvalues = eigenvalues[elements]
eigenvectors = eigenvectors[:,elements]

fix, ax = plt.subplots(figsize=(3, 8))
[ax.plot(  [0, 1], [val, val], 'k-'  ) for val in eigenvalues]
plt.show()
#-------------------------------------Eigenmodes-------------------------------------#

state = 50
normal = 1000  ## factor between the probability and the dot radius in the plot

fig2, ax =plt.subplots()
ax.set_title("Eigenmode Spectrum for 5 x 5 ", fontsize=20, **csfont)
plt.xlabel('Armchair Direction', fontsize=17.5, **csfont)
plt.ylabel('Zig Zag Direction', fontsize=17.5, **csfont)
ax.scatter(positions[:,0], positions[:,1],s=normal*abs(eigenvectors[:,state])**2)
plt.plot()
#-------------------------------------DOS-------------------------------------#
n = 100
En = np.linspace(-3, 3, n)
b=10E-2

def Lorentzian(En,vals,b):
    a = (En - vals)/(b/2)
    return (2 / (np.pi * b)) / (1+a**2)

def DOS(En, vals, b, n):
    dos = np.zeros([n])
    for eig in vals:
        dos += Lorentzian(En, eig, b)
    return dos/len(vals)

csfont = {'fontname':'Times New Roman'}
plt.plot(En, DOS(En, vals, b, n),label="$D(E)$", c='black')
plt.xlabel("E",fontsize=18, **csfont)
plt.ylabel("D(E)",fontsize=18, **csfont)
plt.title("Density of States (DOS) - Finite Model", fontsize=20, **csfont)
plt.axvline(0, c='gray',ls='--', lw=1)
plt.axhline(0.04, c='gray',ls='--', lw=1)
plt.legend(loc='best', fontsize=10)
plt.show()
```

iv. Code: Bandstructures

```python
#------------------Band Structure in the First Brilloiun Zone-----------------#
epsilon = 0
t = -1
a = 1
S = 50

#reciprocal space
b1 = np.array([np.pi / a*np.sqrt(3), 0])
b2 = np.array([0, np.pi / a])
bx = b1[0]
by = b2[1]

#Nearest neighbour vectors
d1 = a * np.array((-1, 0))
d2 = a/2 * np.array((1, np.sqrt(3)))
d3 = a/2 * np.array((1, -np.sqrt(3)))

def Hopping(k, r):
    Hops = t * np.exp(1j * np.dot(k, r))
    return Hops

def HoppingConj(k, r):
    Hops_Conj = t * np.exp(-1j * np.dot(k, r))
    return Hops_Conj

def Hamiltonian(k):
    H = np.matrix([[epsilon, Hopping(k, d1) + Hopping(k, d2) + Hopping(k, d3)],
                    [HoppingConj(k, d1) + HoppingConj(k, d2) + HoppingConj(k, d3),
                    epsilon]])
    Eig = np.real(np.linalg.eigvals(H))
    return Eig

k = [(kx, kx/np.sqrt(3)) for kx in np.linspace(0, bx, 50)]

csfont = {'fontname':'Times New Roman'}

fig = plt.figure(figsize=(10,10))
axis = fig.add_subplot(111, projection='3d')
axis.set_title("3D Bandstructure of Graphene", fontsize=26, **csfont, fontweight='bold')
plt.xlabel('kx', fontsize=20, **csfont,fontweight='bold')
plt.ylabel('ky', fontsize=20, **csfont, fontweight='bold')
axis.set_zlabel('E(k)',fontsize=20, **csfont, fontweight='bold')

kx = np.linspace(-2*bx, 2*bx, S)
ky = np.linspace(-2*bx/np.sqrt(3), 2*bx/np.sqrt(3), S)
X, Y = np.meshgrid(kx, ky)

Z = np.array(list(map(Hamiltonian, zip(X.flatten(), Y.flatten()))))
axis.plot_surface(X, Y, Z[:,0].reshape((S,S)), cmap=cm.Greys)
axis.plot_surface(X, Y, Z[:,1].reshape((S,S)), cmap=cm.Purples);
axis.xaxis.pane.fill = False
axis.yaxis.pane.fill = False
axis.zaxis.pane.fill = False
axis.xaxis.pane.set_edgecolor('w')
axis.yaxis.pane.set_edgecolor('w')
axis.zaxis.pane.set_edgecolor('w')
axis.grid(False)
```

v. Code: Strain Geometries

```python
#-----------------------------------StrainParameters---------------------------------#
A = 10E-10
x0 = 1E-8
y0 = 1.2E-8


y00 = 3.8E-8#2.2E-8


sigma = 0.35E-8 #7.5E-9
cutoff = 20


#Creates array of 0's with identical dimensions as xcoords
GaussianBubble = np.zeros_like(xcoords)
GaussianRipple = np.zeros_like(xcoords)
SinusoidalRipple = np.zeros_like(4*xcoords)


#Gaussian Bubble
R_GB = np.sqrt((xcoords - x0)**2 + (ycoords -y0)**2)
#Gaussian Ripple
R_GR = np.sqrt((ycoords - x0)**2)
R_GRR = np.sqrt((ycoords - y00)**2)


inside_GB = np.where(R_GB < cutoff)
inside_GR = np.where(R_GR < cutoff)
#inside_SR = np.where(R_SR < cutoff)

#-----------------------------------StrainFunctions----------------------------------#

GaussianBubble[inside_GB] =((1.0 / (2 * np.pi * sigma**2)) * A * np.exp(- R_GB[inside_GB]**2
                                                                / (2 * sigma**2)))



GaussianRipple[inside_GR] =((1.0 / (2 * np.pi * sigma**2)) * np.exp(- R_GR[inside_GR]**2
                                                                / (2 * sigma**2)))



SinusoidalRipple[inside_GR] =((1.0 / (2 * np.pi * sigma**2)) * np.exp(- R_GR[inside_GR]**2
                                                                / (2 * sigma**2)))
        + ((1.0 / (2 * np.pi * sigma**2)) * np.exp(- R_GRR[inside_GR]**2 / (2 * sigma**2)))

#-----------------------------------PlottingStrainGeometry---------------------------#
fig = plt.figure(figsize=(5,5))
ax = fig.add_subplot(projection='3d')
ax.scatter(xcoords, ycoords, {strain-function}, s=5, c='black')
plt.xlabel('X')
plt.ylabel('Y')
# Get rid of colored axes planes
# First remove fill
ax.xaxis.pane.fill = False
ax.yaxis.pane.fill = False
ax.zaxis.pane.fill = False

# Now set color to white (or whatever is "invisible")
ax.xaxis.pane.set_edgecolor('w')
ax.yaxis.pane.set_edgecolor('w')
ax.zaxis.pane.set_edgecolor('w')

# Bonus: To get rid of the grid as well:
ax.grid(False)

plt.show()
```

vi. Code: Continuum Dirac model

```python
#-------------------------Preamble/Constants/Strainparameters------------------------#
area = 100E-9
sigma_x = 15E-9
sigma_y = 10E-9
Height = 1E-9
FWHM_y = 2 * np.sqrt(2* np.log(2)) * sigma_y
FWHM_x = 2 * np.sqrt(2* np.log(2)) * sigma_x
x0 = 0
x00 = 0
y0 = 0
y00 = 0


#----------------------------Gridspace/2Dplotspace-----------------------------------#

xl = np.linspace(-area/2, area/2, 250)
yl = np.linspace(-area/2, area/2, 250)
dx = xl[1] - xl[0]
dy = yl[1] - yl[0]

x, y = np.meshgrid(xl, yl)
xx = np.arange(-area/2, area/2 , dx)

PseudoScalarConst = 3
PseudoGaugeConst = -(constants.hbar * 3.37) / (2 * 0.142E-9 * constants.e)

R_x = (x -x0)**2
R_y = (y - y0)**2
R_rs = (y - y00)**2
R_xx = (xx - x0)**2
R_rsxx = (xx - x00)**2

#------------------------------DisplacementVectors-----------------------------------#

def GaussianFold(A, sigma_y, R_y):
    return A * np.exp(-R_y / (2 * sigma_y**2))

def GaussianBubble(A, sigma_x, sigma_y, R_x, R_y):
    return A * np.exp(-(R_y) / (2*sigma_y**2) -(R_x) / (2*sigma_x**2))

#--------------------------------StrainFields----------------------------------------#

def OutOfPlaneStrain(z, dx, dy):
    gradient = np.gradient(z, dx, dy)
    epsxx = 0.5*gradient[1]*gradient[1]
    epsyy = 0.5*gradient[0]*gradient[0]
    epsxy = 0.5*gradient[0]*gradient[1]
    return epsxx, epsyy, epsxy

def PseudoScalarPotential(const, epsxx, epsyy):
    phi = const * (epsxx + epsyy)
    return phi

def PseudoGaugeField(const, epsxx, epsyy, epsxy):
    Ax = const * (epsxx - epsyy)
    Ay = const * (-2*epsxy)
    return Ax, Ay
```

```python
def PseudoMagneticField(Ay, Ax, dx, dy):
    B = np.gradient(Ay, dx, dy)[1] - np.gradient(Ax, dx, dy)[0]
    return B

def TwoDPlot(Z, sigma_y, const, dx):
    gradient = np.gradient(Z, dx)
    eps = 0.5*gradient*gradient
    PSP = const*(eps)
    B = np.gradient(PSP, dx)
    return PSP, B

#--------------------------------CallingFunctions----------------------------------#

#Strain profiles
GF = GaussianFold(Height, sigma_y, R_y)
GB = GaussianBubble(Height, sigma_x, sigma_y, R_x, R_y)
RS = GaussianFold(Height, sigma_y, R_y) + GaussianFold(Height, sigma_y, R_rs)


#--------------------------------MeshStrainProfiles--------------------------------#

fig = plt.figure(figsize=plt.figaspect(0.35))

ax = fig.add_subplot(1,2,1,projection='3d')
plt.title("{TITLE OF STRAIN}")
ax.scatter(x, y, {FUNCTION}, s=0.15, cmap=cm.viridis)

ax = fig.add_subplot(1,2,2)
plt.title("Contour Of Strain Profile",fontsize=20, **csfont, fontweight='bold', y=1.1)
strain_ = ax.pcolormesh(x, y, {FUNCTION}, cmap = cm.inferno, shading='auto')
ax.set_aspect('equal')
plt.xlabel("x",fontsize=18, **csfont)
plt.ylabel("y",fontsize=18, **csfont)
cbar = plt.colorbar(strain_)
cbar.set_label('nm', rotation=0,fontsize=18, **csfont)

fig.tight_layout()
plt.show()

#--------------------------------PGFs/PSFs---------------------------------#
OPS = OutOfPlaneStrain({FUNCTION}, dx, dy)
PSP = PseudoScalarPotential(PseudoScalarConst, OPS[0], OPS[1])
PGF = PseudoGaugeField(PseudoGaugeConst, OPS[0], OPS[1], OPS[2])

Q = 5

fig = plt.figure(figsize=plt.figaspect(0.35))

ax = fig.add_subplot(1,2,1)
plt.title("{TITLE OF FUNCTION}",fontsize=20, **csfont, fontweight='bold', y=1.1)
arrows = ax.quiver (x[::Q, ::Q], y[::Q, ::Q], PGF[0][::Q, ::Q], PGF[1][::Q, ::Q],
                                                      color='blue')
ax.set_aspect('equal')
plt.xlabel("x",fontsize=18, **csfont)
plt.ylabel("y",fontsize=18, **csfont)
ax = fig.add_subplot(1,2,2)
plt.title("Pseudo Scalar Field",fontsize=20, **csfont, fontweight='bold', y=1.1)
ScalerF = ax.pcolormesh(x, y, PSP, cmap = cm.plasma, shading='auto')
ax.set_aspect('equal')
plt.xlabel("x",fontsize=18, **csfont)
plt.ylabel("y",fontsize=18, **csfont)
```

```
cbar = plt.colorbar(ScalerF)
cbar.set_label('$\phi$(meV)', rotation=90,fontsize=18, **csfont)

fig.tight_layout()

plt.show()


#------------------------------------PMFs------------------------------------#

{FUNCTION} = {FUNCTION}(Height, sigma_y, R_xx, ...)
PMF = PseudoMagneticField(PGF[1], PGF[0], dx, dy)
TDP = TwoDPlot(GF, sigma_x, PseudoScalarConst, dx)
maxfield = max (abs(PMF.max() ), abs(PMF.min()) )

fig = plt.figure(figsize=plt.figaspect(0.35))

ax = fig.add_subplot(1,2,1)
plt.title("{TITLE OF FUCNTION}",fontsize=20, **csfont, fontweight='bold', y=1.1)
plt.plot(xx, TDP[0] / sigma_y, color='purple', label='(y)/_y')
plt.plot(xx, -TDP[1], color='red', label='B')
plt.xlabel("y",fontsize=18, **csfont)
plt.ylabel("B(T)",fontsize=18, **csfont)
leg = plt.legend(loc='upper right')

ax = fig.add_subplot(1,2,2)
plt.title("{TITLE OF FUCNTION}",fontsize=20, **csfont, fontweight='bold', y=1.1)
PseudoMagF = ax.pcolormesh (x, y, PMF, cmap = cm.seismic, vmin= -maxfield, vmax= maxfield)
ax.set_aspect('equal')
plt.xlabel("x",fontsize=18, **csfont)
plt.ylabel("y",fontsize=18, **csfont)
cbar = plt.colorbar(PseudoMagF)
cbar.set_label('B(T)', rotation=90,fontsize=18, **csfont)

fig.tight_layout()

plt.show()
```

vii. Code: The Semi-infinite Model

```python
#----------------------------------Nano-Ribbon----------------------------------#

a = 1.42*10E-10   #Lattice constant
acc = a/np.sqrt(3)

Unitcell_x = np.array([0, a/(2*np.sqrt(3)), a*np.sqrt(3)/2, 2*a/np.sqrt(3) ])
Unitcell_y = np.array([0.5*a, 0, 0, 0.5*a])
Unitcell_s = np.array([1,-1,1,-1])

a1 = np.array([np.sqrt(3)*a, 0])
a2 = np.array([0, a])
#-------------------------------------------------------------------------------#

coords_left = x - np.sqrt(3)*a
coords_right = x + np.sqrt(3)*a


fig, ax = plt.subplots()
ax.set_aspect('equal')
ax.set_title("4-sublattice Unit Cell", fontsize=20, **csfont)
plt.xlabel('Armchair Direction', fontsize=17.5, **csfont)
plt.ylabel('Zig Zag Direction', fontsize=17.5, **csfont)
ax.plot(Unitcell_x, Unitcell_y, 'o--',c='purple', markersize=20)
ax.plot(Unitcell_x[1], Unitcell_y[1], 'o--',c='black', markersize=20)
ax.plot(Unitcell_x[3], Unitcell_y[3], 'o--',c='black', markersize=20)
ax.arrow(0, 0, a1[0], a1[1],fc='black',ec='black', width=0.2*10E-10)
ax.arrow(0, 0, a2[0], a2[1],fc='black',ec='black', width=0.2*10E-10)
ax.spines['top'].set_visible(False)
ax.spines['right'].set_visible(False)
plt.show()

#Sheet dimensions
n_x = 15
n_y = 15
x = np.array([])
y = np.array([])
sublattice = np.array([])
for i in np.arange(n_x):
    for j in np.arange(n_y):
        x = np.concatenate( (x,  Unitcell_x + i * a1[0] + j* a2[0]) )
        y = np.concatenate( (y,  Unitcell_y + i * a1[1] + j *a2[1]))
        sublattice = np.concatenate ( (sublattice, Unitcell_s))
fig, ax = plt.subplots()
ax.set_aspect('equal')
ax.set_title("Nano-Ribbon Graphene Model", fontsize=20, **csfont, x= 0.55, y=1.1)
plt.xlabel('Armchair Direction', fontsize=17.5, **csfont)
plt.ylabel('Zig Zag Direction', fontsize=17.5, **csfont)
ax.plot(x[np.where(sublattice==1)], y[np.where(sublattice==1)], 'o',
                                                markersize=4,c='purple')
ax.plot(x[np.where(sublattice==-1)], y[np.where(sublattice==-1)], 'o',
                                                markersize=4,c='black')

ax.plot(coords_right[np.where(sublattice==1)], ycoords[np.where(sublattice==1)], 'x', \par
                                        markersize=4, c = 'purple')
ax.plot(coords_right[np.where(sublattice==-1)], ycoords[np.where(sublattice==-1)], 'x', \par
                                        markersize=4, c = 'black')

ax.plot(coords_left[np.where(sublattice==1)], ycoords[np.where(sublattice==1)], 'x', \par
                                        markersize=4, c = 'purple')
ax.plot(coords_left[np.where(sublattice==-1)], ycoords[np.where(sublattice==-1)], 'x', \par
                                        markersize=4, c = 'black')
```

```python
centre = np.array((xcoords, ycoords)).T
left = np.array((coords_left, ycoords)).T
right = np.array((coords_right, ycoords)).T


def DistanceMatrix(coords_1, coords_2, acc, t0):
    dist = distance_matrix(coords_1, coords_2)
    hops=np.isclose(dist, acc)
    H = -t0 * hops
    return dist, hops, H


def EigenSoln(H):
    vals, vecs = np.linalg.eig(H)
    el = vals.argsort()
    vals = vals[el]
    vecs = vecs[:,el]
    return vals, vecs


CC = DistanceMatrix(centre, centre, acc, t0)
CL = DistanceMatrix(centre, left, acc, t0)
CR = DistanceMatrix(centre, right, acc, t0)
ES = EigenSoln(CC[2])

fix, ax = plt.subplots(figsize=(3, 8))
[ax.plot(  [0, 1], [val, val], 'k-'  ) for val in ES[0]]
plt.show()

kx = np.linspace (-3, 3, 2000)


def Hamiltonian(kx, t0, hops, hopsl, hopsr, d):

    H = t0 * hops + t0 * hopsl *np.exp(-1j * kx * d ) + t0 * hopsr *np.exp(1j * kx * d )

    evals=np.linalg.eigvalsh(H)

    return evals

full_evals=[]

for k in kx:
    evals = Hamiltonian(k, t0, CC[1], CL[1], CR[1], np.sqrt(3)*a)
    full_evals.append(evals)

full_evals = np.array(full_evals)


csfont = {'fontname':'Times New Roman'}

plt.title("Electronic Bandstructure ", fontsize=20, **csfont, fontweight='bold', y=1.1)
[plt.plot(kx, full_evals[:, i], 'k') for i in np.arange(len(centre))]
plt.xlabel('Kx',fontsize=18, **csfont, fontweight='bold')
plt.ylabel('E(k)', fontsize=18, **csfont, fontweight='bold')
plt.show()
```

```python
#----------------------------------StrainParameters----------------------------------#
kx = np.linspace (-3, 3, 2000)
ky = np.linspace (-3, 3, 2000)
A = 3
B = 3.37
a = 1
sigma_x = 10
sigma_y = 15


#Fold parameters
R_xc = (ycoords - y0)**2
R_xcc = (ycoords - y00)**2
R_xl = (coords_left - x0)**2
R_xr = (coords_right - x0)**2


#------------------------------AcquiringStrainCoords----------------------------------#

def GaussianFold(A, sigma_x, R_x):
    return A * np.exp(-R_x / (2 * sigma_x**2))

RS =  GaussianFold(A, sigma_x, R_xc) + GaussianFold(A, sigma_x, R_xcc)


strain_centre = np.array([xcoords, ycoords, GaussianFold(A, sigma_x, R_xc)]).T
strain_right = np.array([coords_right, ycoords, GaussianFold(A, sigma_x, R_xc) ]).T
strain_left = np.array([coords_left, ycoords, GaussianFold(A, sigma_x, R_xc) ]).T

strain_centre1 = np.array([xcoords, ycoords, RS]).T
strain_right1 = np.array([coords_right, ycoords, RS ]).T
strain_left1 = np.array([coords_left, ycoords, RS ]).T

#------------------------------DistanceMatrices/NNHopping----------------------------#
def StrainDistanceMatrix(coords_1, coords_2, strain_1, strain_2, acc):
    dist = distance_matrix(coords_1, coords_2)
    zdist = distance_matrix(strain_1, strain_2)
    hops=np.isclose(dist, acc)
    return dist, zdist, hops

def StrainHopping(zdist, B, t0, acc):
    return t0 * np.exp(-B *((zdist - acc) / acc))
#------------------------------------Hamiltonian-------------------------------------#
def StrainHamiltonian(kx, tc, tl, tr, hops, hopsl, hopsr, d):

    H = tc * hops + tl * hopsl *np.exp(-1j * kx * d ) + tr * hopsr *np.exp(1j * kx * d )

    evals = np.linalg.eigvalsh(H)
    return evals

def StrainHamiltonian2(kx, tc, tl, tr, hops, hopsl, hopsr, d):

    H = tc * hops + tl * hopsl *np.exp(-1j * kx * d ) + tr * hopsr *np.exp(1j * kx * d )

    evals, evecs  = np.linalg.eigh(H)
    return evals, evecs
```

```python
#-----------------------------CallingStrainGeometryFunctions-----------------------------#
#Repeat for other strain geometries outlined
CS = StrainDistanceMatrix(strain_centre[:, 0:2], strain_centre[:, 0:2],
                                          strain_centre, strain_centre, acc)
CLS = StrainDistanceMatrix(strain_centre[:, 0:2], strain_left[:, 0:2],
                                           strain_centre, strain_left, acc)
CRS = StrainDistanceMatrix(strain_centre[:, 0:2], strain_right[:, 0:2],
                                           strain_centre, strain_right, acc)

tc = StrainHopping(CS[1], B, t0, acc)
tl = StrainHopping(CLS[1], B, t0, acc)
tr = StrainHopping(CRS[1], B, t0, acc)

strain_evals=[]

for k in kx:
    s_evals = StrainHamiltonian(k, tc, tl, tr, CS[2], CLS[2], CRS[2], np.sqrt(3)*a)
    strain_evals.append(s_evals)

strain_evals = np.array(strain_evals)

H_s = CS[2]*tc
H_sval = np.linalg.eigvalsh(H_s)

csfont = {'fontname':'Times New Roman'}
fix, ax = plt.subplots(figsize=(3, 8))
plt.ylabel('Energy (eV)', fontsize=17.5, **csfont)
[ax.plot(  [0, 1], [val, val], 'k-', c='r' ) for val in H_sval]
[ax.plot(  [0, 1], [val, val], 'k-'  ) for val in ES[0]]

plt.show()

[plt.plot(kx, strain_evals[:, i], 'k', c='r') for i in np.arange(len(centre))]
[plt.plot(kx, full_evals[:, i], 'k') for i in np.arange(len(centre))]

plt.title("Gaussian Fold", fontsize=20, **csfont, fontweight='bold', y=1.1)
plt.xlabel('Kx',fontsize=18, **csfont, fontweight='bold')
plt.ylabel('E(k)', fontsize=18, **csfont, fontweight='bold')
plt.show()

band = int(len(centre)/2)

kspec = 0.15
kspec1 = -0.15
[plt.plot(kx, strain_evals[:, i], 'k') for i in np.arange(len(centre))]
plt.plot(kx, strain_evals[:, band], 'r')
plt.plot(kspec, StrainHamiltonian(kspec, tc, tl, tr, CS[2], CLS[2], CRS[2], np.sqrt(3)*a)
                                                                   [band], 'ro')
plt.plot(kspec1, StrainHamiltonian(kspec1, tc, tl, tr, CS[2], CLS[2], CRS[2], np.sqrt(3)*a)
                                                                   [band], 'bo')
plt.show()

R_xc1 = (avy-y0)**2

def GaussianFold1(A, sigma_x, R_x):
    return A * np.exp(-R_x / (2 * sigma_x**2))
GF = GaussianFold1(A, sigma_x, R_xc1)

avy = np.convolve(ycoords[shortlist], np.ones((3,))/3, mode='valid')
avprob = np.convolve(projection[shortlist], np.ones((3,))/3, mode='valid')
```

```python
fig = plt.figure()

ax1= fig.add_subplot(211)
pl = ax1.scatter(avy1, avprob1, c=avprob1, cmap="Reds", s=30, edgecolors="black")
ax2=fig.add_subplot(212)
ax2.plot(avy1, GF, c='black')

fig.subplots_adjust(right=0.8)
cbar_ax = fig.add_axes([0.85, 0.15, 0.05, 0.7])
fig.colorbar(pl, cax=cbar_ax)

# plt.colorbar(pl)
# pl.set_label('X+Y')
plt.title("Gaussian Fold", fontsize=20, **csfont, fontweight='bold',x = -7.7, y=1.1)

plt.show()
```
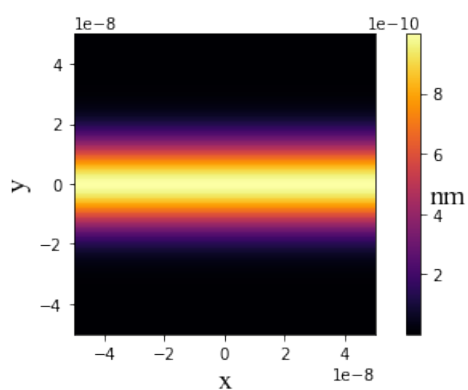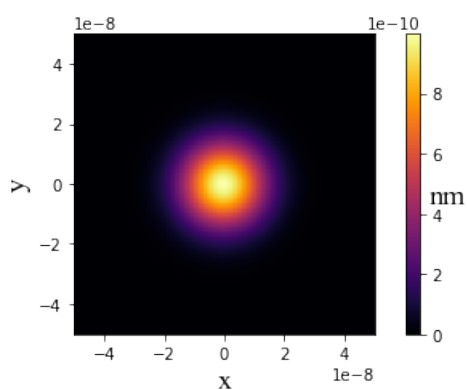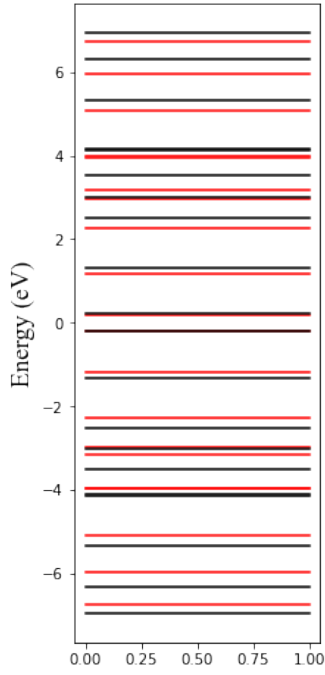
viii. Contour of Strain Profiles
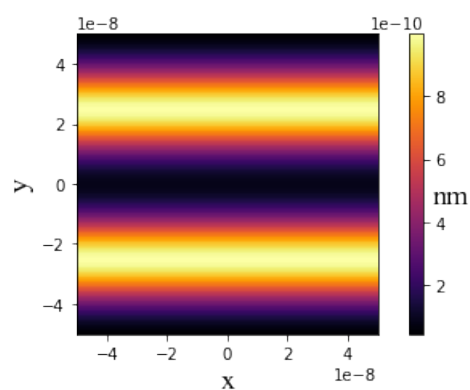
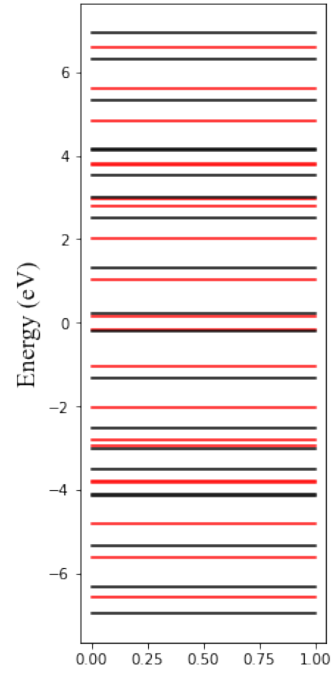**Figure 2.8** Contour of strain profiles outlined in fig. 1.9.
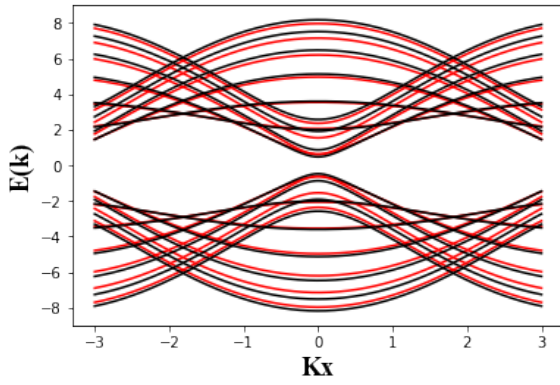
(a)

(b)

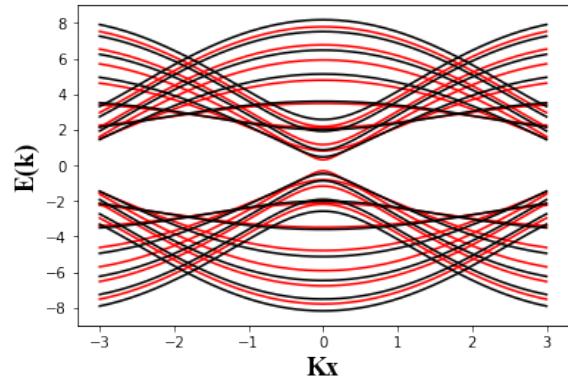**Gaussian Fold**

Double Fold

(c)

(d)

Figure 2.9 Strained bandsstructure and alternated energy levels utilising the semi-infinite model for $n_y = 5$

References

[1] Wallace P. Erratum: The Band Theory of Graphite [Phys. Rev. 71, 622 (1947)]. Physical Review. 1947;72(3):258-258

[2] Boehm H, Clauss A, Fischer G, Hofmann U. Das Adsorptionsverhalten sehr d¨unner Kohlenstoff-Folien. Zeitschrift f¨ur anorganische und allgemeine Chemie. 1962;316(3- 4):119-127.

[3] Ruess G, Vogt F. H¨uchstlamellarer Kohlenstoff aus Graphitoxyhydroxyd. Monatshefte f¨ur Chemie. 1948;78(3-4):222-242.

[4] Boehm H, Setton R, Stumpp E. Nomenclature and terminology of graphite intercalation compounds. Carbon. 1986;24(2):241-245.

[5] Grant J, Haas T. Auger electron spectroscopy of Si. Surface Science. 1970;23(2):347-362.

[6] Blakely J, Kim J, Potter H. Segregation of Carbon to the (100) Surface of Nickel. Journal of Applied Physics. 1970;41(6):2693-2697.

[7] Novoselov K, Geim A, Morozov S, Jiang D, Zhang Y, Dubonos S et al. Electric Field Effect in Atomically Thin Carbon Films. Science. 2004;306(5696):666-669.

[8] Graphene - Wikipedia [Internet]. En.wikipedia.org. 2021. Available from: https://en.wikipedia.org/wiki/Graphenecitenote-novo2004-13

[9] Lee J, Yoon D, Cheong H. Estimation of Young's Modulus of Graphene by Raman Spectroscopy. Nano Letters. 2012;12(9):4444-4448.

[10] Cooper D, D'Anjou B, Ghattamaneni N, Harack B, Hilke M, Horth A et al. Experimental Review of Graphene. ISRN Condensed Matter Physics. 2012;2012:1-56.

[11] Pereira V, Castro Neto A, Peres N. Tight-binding approach to uniaxial strain in graphene. Physical Review B. 2009;80(4).

[12] Katsnelson M, Novoselov K. Graphene: New bridge between condensed matter physics and quantum electrodynamics. Solid State Communications. 2007;143(1-2):3-13.

[13] Kim P. Graphene and Relativistic Quantum Physics. 2014;:3 - 6.

[14] Han C, Xu H, Lai Y. Pseudospin modulation in coupled graphene systems. Physical Review Research. 2020;2(3).

[15] Georgi A, Nemes-Incze P, Carrillo-Bastos R, Faria D, Kusminskiy S, Zhai D et al. Correction to Tuning the Pseudospin Polarization of Graphene by a Pseudomagnetic Field. Nano Letters. 2018;18(10):6654-6654.

[16] Xu H, Huang L, Lai Y. Relativistic quantum chaos in graphene. Physics Today. 2021;74(2):44-49. [17] Katsnelson M, Novoselov K, Geim A. Chiral tunnelling and the Klein paradox in graphene. Nature Physics. 2006;2(9):620-625.

[18]Pereira V, Castro Neto A, Peres N. Tight-binding approach to uniaxial strain in graphene. Physical Review B. 2009;80(4).

[19] Ni Z, Yu T, Lu Y, Wang Y, Feng Y, Shen Z. Uniaxial Strain on Graphene: Raman Spectroscopy Study and Band-Gap Opening. ACS Nano. 2009;3(2):483-483.

[20] Choi S, Jhi S, Son Y. Effects of strain on electronic properties of graphene. Physical Review B. 2010;81(8).

[21] Yang L, Han J. Electronic Structure of Deformed Carbon Nanotubes. Physical Review Letters. 2000;85(1):154-157.

[22] Carrillo-Bastos R, Ochoa M, Zavala S, Mireles F. Enhanced asymmetric valley scattering by scalar fields in nonuniform out-of-plane deformations in graphene. Physical Review B. 2018;98(16).

[23] Milovanović S, Peeters F. Strain controlled valley filtering in multi-terminal graphene structures. Applied Physics Letters. 2016;109(20):203108.

[24] Cavalcante L, Chaves A, da Costa D, Farias G, Peeters F. All-strain based valley filter in graphene nanoribbons using snake states. Physical Review B. 2016;94(7).

[25] Geim A, Novoselov K. The rise of graphene. Nature Materials. 2007;6(3):183-191.

[26] Neto A, Guinea F, Peres N. Drawing conclusions from graphene. Physics World. 2006;19(11):33-37.

[27] Zheng Y, Valerio G, Ren Z. Effect of mechanical stresses on graphene-based devices. International Journal of Numerical Modelling: Electronic Networks, Devices and Fields. 2017;31(2):e2233.

[28] Schaibley J, Yu H, Clark G, Rivera P, Ross J, Seyler K et al. Valleytronics in 2D materials. Nature Reviews Materials. 2016;1(11).

[29] 14. Xiao D, Yao W, Niu Q. Valley-Contrasting Physics in Graphene: Magnetic Moment and Topological Transport. Physical Review Letters. 2007;99(23).

[30] Low T, Guinea F. Strain-Induced Pseudomagnetic Field for Novel Graphene Electronics. Nano Letters. 2010;10(9):3551-3554.

[31] McCann E. Electronic properties of monolayer and bilayer graphene. Lancaster University, Lancaster, LA1 4YB, United Kingdom; 2012.

[32] Slonczewski J, Weiss P. Band Structure of Graphite. Physical Review. 1958;109(2):272-279.

[33] McEuen P, Bockrath M, Cobden D, Yoon Y, Louie S. Disorder, Pseudospins, and Backscattering in Carbon Nanotubes. Physical Review Letters. 1999;83(24):5098-5101.

[34] Zhai D, Sandler N. Local versus extended deformed graphene geometries for valley filtering. Physical Review B. 2018;98(16).

[35] Vozmediano M, Katsnelson M, Guinea F. Gauge fields in graphene. Physics Reports. 2010;496(4-5):109-148.

Rickhaus P, Makk P, Liu M, Tóvári E, Weiss M, Maurand R et al. Snake trajectories in ultraclean graphene p–n junctions. Nature Communications. 2015;6(1).

[36] Müller J. Effect of a nonuniform magnetic field on a two-dimensional electron gas in the ballistic regime. Physical Review Letters. 1992;68(3):385-388.

[37] Oroszlány L, Rakyta P, Kormányos A, Lambert C, Cserti J. Theory of snake states in graphene. Physical Review B. 2008;77(8).

[38] Chen J, Xie X, Sun Q. Current oscillation of snake states in graphenep-njunction. Physical Review B. 2012;86(3).

[39] Slater J, Koster G. Simplified LCAO Method for the Periodic Potential Problem. Physical Review. 1954;94(6):1498-1524.

[40] Lu B. The Casimir Effect in Topological Matter. Universe. 2021;7(7):237.

[41] N.W. Ashcroft, N.D. Mermin, Solid-State Physics, (Brooks/Cole, Belmont, 1976)

[42] Balkanski M. Physical Properties of Carbon Nanotubes, Edited by R. Saito, G. Dresselhaus and M.S. Dresselhaus, Imperial College Press, London, 1998. Materials Science and Engineering: B. 2000;76(3):241-242.

[43] Kittel C, McEuen P. Introduction to solid state physics. Hoboken, NJ: John Wiley Sons; 2019. [44] Biczó G. On the self-consistent-field linear combination of atomic orbitals for bounded crystal orbitals (SCF-LCAO-BCO) method. Journal of Molecular Structure: THEOCHEM. 1989;188(3-4):429-439.

[45] Fuchs J, Goerbig M. Introduction to the Physical Properties of Graphene. 2008;:21-24.

[46] Lu G, Yu K, Wen Z, Chen J. Semiconducting graphene: converting graphene from semimetal to semiconductor. Nanoscale. 2013;5(4):1353.

[47] Hobson J, Nierenberg W. The Statistics of a Two-Dimensional, Hexagonal Net. Physical Review. 1953;89(3):662-662. [48] Cayssol J. Introduction to Dirac materials and topological insulators. Comptes Rendus Physique. 2013;14(9-10):760-778. [49] Carrillo-Bastos R, Faria D, Latgé A, Mireles F, Sandler N. Gaussian deformations in graphene ribbons: Flowers and confinement. Physical Review B. 2014;90(4).

[50] Zhai D, Sandler N. Local versus extended deformed graphene geometries for valley filtering. Physical Review B. 2018;98(16).

[51] Jia P, Chen W, Qiao J, Zhang M, Zheng X, Xue Z et al. Programmable graphene nanobubbles with three-fold symmetric pseudo-magnetic fields. Nature Communications. 2019;10(1).

[52] Landau L, Lifsic E. Theory of elasticity. Amsterdam: Elsevier; 2008.

[53] Castro Neto A, Guinea F. Electron-phonon coupling and Raman spectroscopy in graphene. Physical Review B. 2007;75(4).

[54] D. A. Papaconstantopoulos, M. J. Mehl, S. C. Erwin, and M. R. Pederson, in Tight-Binding Approach to Computational Materials Science, edited by P. Turchi, A. Gonis, and L. Colombo Materials Research Society, Pittsburgh, 1998, p. 221. [55] Jones G, Pereira V. Designing electronic properties of two-dimensional crystals through optimization of deformations. New Journal of Physics. 2014;16(9):093044.

[56] Pereira V, Castro Neto A. Strain Engineering of Graphene's Electronic Structure. Physical Review Letters. 2009;103(4). Suzuura H, Ando T. Phonons and electron-phonon scattering in carbon nanotubes. Physical Review B. 2002;65(23).

[57] Kim K, Blanter Y, Ahn K. Interplay between real and pseudomagnetic field in graphene with strain. Physical Review B. 2011;84(8).

[58] Wakker G, Tiwari R, Blaauboer M. Localization and circulating currents in curved graphene devices. Physical Review B. 2011;84(19).

[59] Levy N, Burke S, Meaker K, Panlasigui M, Zettl A, Guinea F et al. Strain-Induced Pseudo–Magnetic Fields Greater Than 300 Tesla in Graphene Nanobubbles. Science. 2010;329(5991):544-547. [60] Sasaki K, Saito R. Pseudospin and Deformation-Induced Gauge Field in Graphene. Progress of Theoretical Physics Supplement. 2008;176:253-278. [61] Banerjee R, Nguyen V, Granzier-Nakajima T, Pabbi L, Lherbier A, Binion A et al. Strain Modulated Superlattices in Graphene. Nano Letters. 2020;20(5):3113-3121.

[62] Hartmann R, Robinson N, Portnoi M. Smooth electron waveguides in graphene. Physical Review B. 2010;81(24).

[63] Carrillo-Bastos R, León C, Faria D, Latgé A, Andrei E, Sandler N. Strained fold-assisted transport in graphene systems. Physical Review B. 2016;94(12).

[64] Mucciolo E, Lewenkopf C. Disorder and electronic transport in graphene. Journal of Physics: Condensed Matter. 2010;22(27):273201.